TOTAL CROSS SECTION MEASUREMENTS FOR $^{3}He(^{3}He, 2p)^{4}He$ AT LOW ENERGIES

Thesis by

Mirmira Ramarao Dwarakanath

In Partial Fulfillment of the Requirements

For the Degree of

Doctor of Philosophy

California Institute of Technology

Pasadena, California

1969

(Submitted May 25, 1968)

ACKNOWLEDGMENTS

I wish to thank the faculty, staff and students of the Kellogg Radiation Laboratory for providing such an exciting and delightful atmosphere in which to learn. It is a pleasure to thank Professor William A. Fowler for his keen interest in these measurements and the encouragement he has given throughout the course of this work.

I am particularly indebted to Dr. Hubert C. Winkler, who not only actively participated in these measurements, but also had worked out many of the details of the experiment even before my association with the project. It was a very pleasurable and rewarding experience to work with Dr. Winkler who introduced me to many of the techniques of low energy nuclear physics. It is a sincere pleasure to thank Professor Thomas A. Tombrello for his guidance throughout my association with him and for the many valuable discussions and criticisms. I am very grateful to him for having had the opportunity to be one of his students. Greatly appreciated is the patient teaching of Dr. Andrew D. Bacher about this reaction and other facets of experimental research.

The efforts of Mr. Victor F. Erghott in the design of some of the apparatus and the precision work of the personnel in the Kellogg shop in fabricating the experimental apparatus are gratefully acknowledged. The unstinted help given by Mr. Donald L. McGrath in the maintenance of the accelerator and other equipment is much appreciated. My special thanks to Mr. Jerry Jordan and the personnel in the Graphic Arts facility for help with the illustrations and to Mrs. Joan Schuetz for the neat and accurate typing.

I am very grateful to the California Institute of Technology for the generous financial assistance given me throughout my stay at

Caltech. The support given to this project by the Office of Naval Research is thankfully acknowledged.

ABSTRACT

Precise measurements of the total reaction cross section for $^{3}He(^{3}He, 2p)^{4}He$ have been made in the range of center-of-mass energies between 1100 keV and 80 keV. A differentially pumped gas target modified to operate with a limited quantity of the target gas was employed to minimize the uncertainties in the primary energy and energy straggle. Beam integration inside the target gas was carried out by a calorimetric device which measures the total energy spent in a heat sink rather than the total charge in a Faraday cup. Proton energy spectra have been obtained using a counter telescope consisting of a gas proportional counter and a surface barrier detector and angular distributions of these protons have been measured at seven bombarding energies. Cross section factors, S(E), have been calculated from the total cross sections and fitted to a linear function of energy over different ranges of energy. For $E_{cm} < 500$ keV

$$S(E_{cm}) = S_0 + S_1 E_{cm}$$

where $S_0 = (5.0\ ^{+0.6}_{-0.4})$ MeV - barns and $S_1 = (-1.8 \pm 0.5)$ barns.

TABLE OF CONTENTS

I. INTRODUCTION

It was proposed by Bethe and Critchfield (1938) and Bethe (1939) that main sequence stars which consist primarily of hydrogen, derive their energy mainly from two sequences of nuclear reactions each of which have the net effect of converting four hydrogen atoms into a helium atom and two neutrinos with release of energy. One such sequence is the CNO bicycle, the other is the proton-proton chain. The proton-proton chain is believed to be more important in fainter stars, such as our Sun, with lower central temperatures and having low abundance of the catalysts needed for the CNO bicycle.

The proton-proton chain is initiated by the rate determining weak process $^{1}H + {}^{1}H \rightarrow {}^{2}H + e^{+} + \nu$. The deuterium is subsequently converted into ^{3}He by radiative capture of a proton. It was originally believed that the ^{3}He was transformed into ^{4}He by further radiative capture and the β-decay of ^{4}Li. ^{4}Li has since been found to be unstable to particle emission. However, there are other ways in which ^{3}He can be converted into ^{4}He. One such way is the reaction under investigation, viz.

$$^{3}He + {}^{3}He \rightarrow {}^{4}He + {}^{1}H + {}^{1}H + 12.86\ MeV.$$

The role of this reaction in the p-p chain was first suggested by C. C. Lauritsen [quoted by Fowler (1951)] and by Schatzman (1951). It was first observed by Good, Kunz and Moak (1951). This process happens to be the fastest and most important in terminating the proton-proton chain in the Sun.

At the present time the following sequences of reactions [Fowler, 1958] are considered to be the most important in the proton-proton chain.

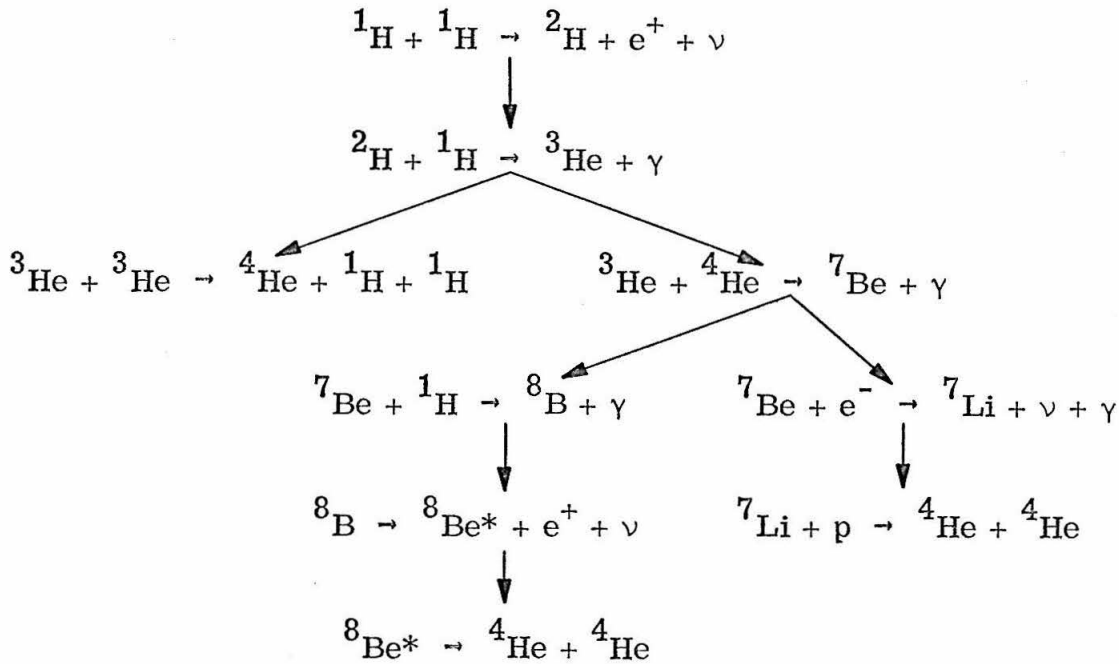

In principle, a stellar model can be constructed to check the validity of these beliefs regarding the process of energy generation in stars. A stellar model is completely determined by its mass and initial composition. However, precise knowledge of the nuclear reaction cross sections under stellar conditions is required in addition to an understanding of other physical processes such as energy transport, etc.. The major nuclear physics uncertainty [Parker, Bahcall and Fowler, 1964] in the calculations of a solar model has been associated with the uncertainty in the

cross section for $^3He + {}^3He \rightarrow {}^4He + 2p$. The present investigation was undertaken to minimize this uncertainty.

The mean thermal energy in the center of Stars like our Sun is a few keV. This energy is extremely small compared to the Coulomb barriers encountered. Since the probability of barrier penetration decreases very rapidly with the energy of the particles, the reaction cross sections also decrease. Consequently, most of the reactions take place over a small range of energies in the tail of the Maxwellian distribution. For the reaction under study, this range of energies is centered around 18.5 keV for a temperature $T = 15 \times 10^6\ ^oK$ which is regarded as the central temperature of the Sun. Thus, the quantity of interest is the reaction cross section in the energy region 10-30 keV for solar model calculations. Technical difficulties preclude such measurements at the present time, since the total cross section is very small in this energy range (estimated to be $\sim 3 \times 10^{-13}$ barn at 20 keV). Therefore, one must extrapolate the low energy data.

In order to extrapolate the rapidly varying cross section the obvious energy dependence, which is also responsible for the fast variation of the cross section with energy, is factored out and the cross section factor is extrapolated. The energy dependence is written as

$$\sigma(E) = S(E)\,\frac{\exp(-2\pi\eta)}{E} \qquad \text{where} \quad \eta = \frac{z_1 z_2 e^2}{\hbar v} \ .$$

The factor $\frac{1}{E} e^{-2\pi\eta}$ contains in it the flux factor $\frac{1}{\sqrt{E}}$, and the remaining $\frac{1}{\sqrt{E}} e^{-2\pi\eta}$ is the barrier penetration factor. The cross section factor, S(E) is a slowly varying function of energy for non-resonant processes.

It is important to be able to extrapolate this cross section factor down to the relevant energies with a good degree of accuracy. Although the reaction cross section for the primary rate determining weak process is the most important nuclear quantity in solar model calculations, the reaction cross sections for the $^3He + ^3He$ and the $^3He + ^4He$ processes together play an important role in the termination of the p-p chain which in turn affects the primary reaction. For example, termination of the chain purely through the $^3He + ^3He$ mode would require twice the number of primary reactions per second as would be necessary to account for the same luminosity with termination through the $^3He + ^4He$ mode alone. In addition, the reaction cross sections strongly influence the branching ratios for the various terminations which in turn affect the flux of high energy neutrinos from the electron capture of ^7Be and the β-decay of ^8B inside the Sun. Changes in these ratios would greatly affect the significance of the results from the neutrino observatory [Davis, 1964] where experiments are underway to detect these high energy solar neutrinos.

Previous work - The earliest attempt to obtain the cross section factor for the $^3He + ^3He$ reaction was made from the measurements on the mirror reaction:

$$^3H + ^3H \rightarrow ^4He + 2n + 11.83 \text{ MeV}$$

by Agnew et al. (1951). This reaction being exactly analogous to the $^3He + ^3He$ reaction, it was assumed that the nuclear matrix elements for the two processes would be very nearly equal after the Coulomb effects were factored out. The cross section factors for the two reactions differ primarily due to the way in which the quantity is defined, viz., the cross section factor does not include the product $z_1 z_2$ appearing in the penetration factor for the Coulomb barrier. The measurements of Agnew et al. for the $^3H + ^3H$ reaction over the range of energies 100-500 keV gave for the value of the cross section factor $S = (3.2 \pm 1.5) \times 10^5$ eV-barns [Salpeter, 1952], which implies that $S \sim 1.3 \times 10^6$ eV-barns for the $^3He + ^3He$ process.

The total reaction cross sections for the $^3He + ^3He$ process was first measured by Good, Kunz and Moak (1953). They employed a ^3He target made by bombarding an aluminum foil with an intense beam of 84 keV ^3He ions. The ^3He trapped in the foil was used as the target. Total cross sections were measured by comparing the yield of the reaction under study with the yield from the $^3He(d, p)^4He$ reaction from the same target and using the known values of the $^3He(d, p)^4He$ total cross sections.

The chief uncertainty in their measurements stems from the nature of the target employed which is 84 keV thick for 84 keV ^3He. Such thick target yields can give accurate cross sections only if the exact distribution of the ^3He with depth in the target is known. In addition, it is necessary to know the specific energy loss of ^3He ions in aluminum over the entire range of energies employed. Uncertainties in these details can be regarded as an uncertainty in the primary energy. Any uncertainty in the primary energy appears

as a much larger uncertainty in the cross section factor at the energies studied, because of the rapid change in the cross section with the incident energy. It seems therefore that the results of Good et al. could have large errors associated with them. Further, their measurements exhibit an abrupt change in the energy dependence of the cross section factor which does not lend itself either to easy interpretation or to extrapolation to energies of astrophysical interest.

Bacher and Tombrello [1965, Bacher, 1967] undertook a detailed study of this reaction in the range of bombarding energies 1-20 MeV, to understand the reaction mechanism and to develop a consistent scheme which would allow extending their results at higher energies to measurements at low energies ($\eta > 1$). This reaction is well understood by them as proceeding mainly through an intermediate state of (^{5}Li + p) for bombarding energies greater than 3 MeV. However, they find that this mechanism is inadequate to explain their observations at lower energies. Thus the knowledge gained of the reaction mechanism at higher energies is not fully applicable to low energy measurements, necessitating the work described here.

The experimental techniques of the measurements at higher energies become unsuitable for very low energy measurements of comparable accuracy. The subject of this thesis is a discussion of some low energy, gas target techniques and the study of the reaction ^{3}He(^{3}He, 2p)^{4}He in the range of energies:
160 keV $< E_{^3\mathrm{He}} <$ 2.2 MeV.

Since undertaking this project, Neng-Ming et al. (1966) have reported their investigation of this reaction in the energy range 0.5 to 1.7 MeV. Also Bacher and Tombrello (1967) have continued measurements down to 300 keV with apparatus similar to that used in their higher energy measurements. The results of these groups are discussed in Chapter V.

II. EXPERIMENTAL APPARATUS

A. ^{3}He Beams

The ^{3}He beams employed in these measurements covered the range of energies 2.22 MeV to 160 keV. They were obtained from the 3 MV and the 600 kV electrostatic generators (ESG) of the Van de Graaff type housed in the Caltech Kellogg Radiation laboratory.

The 3 MV ESG provided singly charged ^{3}He beams in the energy range 2.22 MeV to 450 keV. The ^{3}He ions were analyzed by a 90°, 40 cm radius double-focusing magnet. The beam energy resolution was almost entirely determined by the feedback control slit settings. In this case the slit setting was 3 mm corresponding to an energy resolution of better than 1.5%. The existing energy calibration of the 90° analyzing magnet was checked by observing the narrow (Γ = 0.08 keV) 992.0 keV (p,γ) resonance in ^{27}Al with H^+ and $(HH)^+$ beams. The energy calibration differed by four parts in 1000 from the previous energy calibration. This difference has been taken into account in obtaining the beam energies.

For energies in the range of 500-160 keV, singly charged ^{3}He beams were provided by the 600 kV ESG. The ions were analyzed by a 41 cm radius, 90° double-focusing magnet. The energy resolution was again ~ 1.5%. The energy calibration of the analyzer was checked by observing the following resonances:

1) $^{11}B(p,\gamma)^{12}C^*$ - (E_p = 163.1 keV, Γ = 6.3 keV) - with H^+ and $(HH)^+$ beams.
2) $^{19}F(p,\alpha\gamma)^{16}O$ - (E_p = 340.5 keV, Γ = 2.7 keV) - with H^+ and $(HH)^+$ beams.

3) $^{7}Li(p, \gamma)^{8}Be$ - (E_p = 441. 2 keV, Γ = 12. 2 keV) - with only the H^+ beam.

This time the new measurements differed from the existing calibration by 1%. This difference was not unexpected since the control slits had been moved during realignment of the beam tube.

B. Gas Target

Gas targets are generally of two types - 1. The gas cell or 2. The differentially pumped gas target system.

The gas cell employs thin entrance windows to admit the beam while confining the gas to the volume of the cell. The gas cell, very convenient as it is, suffers from serious disadvantages for low energy measurements. This has to do with the energy loss and straggling of the primary beam in traversing the entrance window and the limitation the foil imposes on the maximum beam current. Precise experimental data on helium ion energy losses and straggling are lacking in the energy region of interest. Theoretical results are not directly applicable because of the complex charge exchange processes occurring when these low energy ions traverse matter. Unless accurate measurements of energy losses and straggling are made for the entrance foil used, these uncertainties will become a source of serious errors in the value of the cross section factor.

The differentially pumped gas target system (DPGT) - This device circumvents the need for entrance windows to maintain the pressure difference between the target and accelerator vacuum system by having the target gas flow out of the target through a high

impedance. The target pressure is maintained by feeding gas into the scattering chamber, while the high vacuum is preserved at the entrance to the accelerator by pumping away the gas streaming in. Approximate flow rates of several millimoles/sec are needed to maintain a gas target at a pressure of a few cm of mercury. The flow rates can be cut down at the expense of the beam current by using smaller apertures. For rare gases like ^{3}He the flow rate is prohibitively high if the ^{3}He were continuously exhausted into the atmosphere.

The recirculating DPGT has the added advantage of using a limited quantity of the rare gas; the target gas is recovered from the high vacuum side instead of pumping it out into the atmosphere. The gas is compressed, cleaned of its impurities and fed back into the target chamber. A recirculating differentially pumped gas target system designed for a maximum operating target pressure of $\sim$ 20 torr (20 mm of Hg) will be described below.

The pressure difference between the target region ($\sim$ 20 torr) and the accelerator region ($\sim 10^{-6}$ torr) is achieved in three stages. The main pressure drop occurs across canal-A (see Figures 1 and 2). This canal connects the target region to a large chamber, labeled A, pumped by two Roots type blowers in a cascade. The typical pressure reached in chamber-A is $\sim$ 0.1 torr. Chamber-A is connected to another large chamber-B by a second canal, canal-B. The chamber-B is pumped by an oil diffusion pump whose exhaust is connected to chamber-A. This procedure allows recovery of most of the gas streaming through canal-B which is already quite small compared to the gas flow in canal-A. Pressures in chamber-B are $\sim 10^{-5}$ torr. The pressure here is sufficiently low to allow the accelerator beam tube to be connected

to this region. A third impedance, canal-C is placed in the beam pipe, as shown in the drawings, to further reduce gas leakage into the accelerator vacuum. The output of the last roots pump in the cascade develops a sufficiently high pressure to make possible recirculation of the gas. The gas coming out of the pumps is contaminated by pump oils and possibly by air leaking into the system. This gas is cleaned of its impurities by passing it through an adsorber of zeolite, maintained at liquid nitrogen temperature. The adsorber is a commercial product with the trade name 'VacSorb' manufactured by Varian Associates, Palo Alto, California. This substance has been found to be extremely efficient in cleaning the gas. The chilled gas passing out of the trap is allowed to exchange heat with the incoming gas before it is fed back to the target chamber. (A more detailed description of the recirculating DPGT is given in Appendix 1.)

The canal-A is made re-entrant to minimize the energy loss of the primary beam in reaching the center of the target chamber. The energy loss of the primary beam up to the point of entering canal-A is negligible. Corrections have to be made for the energy loss in traversing the length of the canal and from the tip of the canal to the center of the target chamber. This correction is quite small ($\sim$ 15 keV) and the uncertainty in estimating this is only about 3 keV under the most unfavorable circumstances. The tip of the canal is 7 mm removed from the center of the target chamber, permitting a maximum target thickness of about 1 cm.

The degraded beam - It is essential to minimize the beam scattered from the sides and tip of the canal. This is achieved by having an aperture of a slightly smaller size than

the bore of the canal, at the entrance to the canal, and also by opening out the bore at the exit end. The energy distribution of the beam entering the target chamber was analyzed by observing the spectrum of protons elastically scattered from argon. The fraction of the degraded beam for protons of 1 MeV was less than 0.5%. This would be somewhat higher for ^{3}He.

Pressure measurement - The target density (n_T) or the number of atoms/cm^3 of the target is obtained by measuring the static pressure and the temperature of the gas inside the target chamber. The pressure is continuously monitored by an aneroid type pressure gauge manufactured by Wallace and Tiernan, Inc., Belleville, N. J.. The gauge is calibrated in steps of 0.1 torr and covers the range of pressures 0-20 torr. Pressures can be read from the dial with an accuracy of better than ± 0.05 torr. The instrument calibration was checked by comparing it with an absolute pressure gauge of the McLeod type. No corrections were found necessary.

The pressure in the chamber was not strictly constant over long periods of time. The pressure dropped at a slow rate (at most, a few percent per hour) due to gas loss to the accelerator vacuum and due to internal 'icing' of the zeolite trap which gradually increased its impedance. Pressures were recorded at regular intervals and a time average of the pressure was used as the mean pressure.

C. Beam Integration

Conventional beam integration devices which measure the total charge deposited by the beam in a Faraday cup, are not suitable for beam integration inside gas target chambers because of the ionization of the target gas by the incident beam. Since several ion pairs are created in the gas for every ion in the primary beam, charge integration can be meaningful only if all the charges are collected. That is, integration has to be carried out over the entire target chamber excluding the canal. The real difficulty lies in insuring that there be no net charge transfer from the gas to the canal and in our incomplete knowledge of the charge states of ^{3}He ions after traversing the tenuous matter in the canal.

The difficulties encountered in a conventional device were overcome by measuring the total energy deposited by the beam in a heat sink rather than the total charge. The energy dissipated appears as heat and the quantity of heat released in a low mass, high conductivity material was measured by balancing this quantity against the amount of electrical energy dissipated in a dummy heat sink of similar construction. The amount of electrical energy supplied to the dummy is then a measure of the total energy deposited in the calorimeter by the beam. The proportionality constant differs from unity because of departures from total symmetry in the construction of the calorimeter and dummy heat sinks. (The construction and working of this device are described in detail in Appendix 2.)

The number of incident particles is simply obtained as the ratio of the total energy deposited by the beam to the energy of each ion at the position of the calorimeter.

$$N_B = \frac{C W_E}{(E - \Delta E)}$$

where N_B = the number of incident ions

W_E = the electrical energy supplied to the dummy

C = the calorimeter calibration constant

$C W_E$ = the total energy deposited by the beam in the calorimeter

E = primary beam energy

ΔE = the energy loss suffered by primary beam in passing through the target and canal.

The accuracy of the calorimetric beam integration device has been checked by measuring the proton elastic scattering cross section from argon gas which is primarily argon-40. The $^{40}A(p, p)^{40}A$ scattering has been investigated before [Cohen-Ganouna et al., 1963] and no strong anamolies have been observed for $E_p < 1.8$ MeV. Differential cross sections have been obtained at 130^o and 140^o to the direction of the incident beam. At these angles the measurements are very insensitive to errors in the knowledge of the scattering angle for gas targets. This is because

$\frac{\partial}{\partial\psi}\left[\left.\frac{d\sigma_R}{d\Omega}\right|_{\psi}\langle\Omega\ell\rangle_{\psi}\right]$ vanishes at $\psi \simeq 132^{o}$, where ψ is the scattering angle in the laboratory, $\left.\frac{d\sigma_R}{d\Omega}\right|_{\psi}$ and $\langle\Omega\ell\rangle_{\psi}$ are the Rutherford cross section and the geometrical factor [see Section E, page 17] at an angle ψ.

These measurements together with a few measurements at 90^{o} are compared with the Rutherford cross section in Table 2. The agreement is seen to be very good.

D. Particle Detection

As there are three particles in the final state of the reaction $^{3}He + {}^{3}He \rightarrow {}^{4}He + 2p$, the outgoing particles have continuous energies, from zero energy extending to the three body end point at any fixed angle. In order to distinguish between protons and alpha particles, a measurement of the specific energy loss in matter is necessary in addition to the measured energy of the particles. The total energy and the specific energy loss of a particle are measured by a counter telescope. The reaction products pass through a transmission type (δE) counter before reaching a detector sufficiently thick to stop them. The δE counter which provides a measure of the specific energy loss, also limits the observation of the low energy end of the particle spectra. Hence, it is desirable to have as thin a δE-counter as feasible, to obtain particle spectra down to very low energies. For this reason, the δE-counter in this experiment is a gas proportional counter with a thin entrance window. This entrance foil has approximately the correct thickness to stop the elastically scattered ^{3}He at the highest energy measured.

The proportional counter - The present experiment placed no severe demands on the resolution of the proportional counter since the specific energy loss of alpha particles is several times larger than for protons of the same energy. The requirement that the proportional counter noise be small compared to the signal of the highest energy protons was easily met.

The proportional counter consists of 0.2 mm diameter steel wire stretched between two insulating supports inside an aluminum box of dimensions 6.5 cm x 6.5 cm x 3.0 cm as shown in Figure 3. The steel wire forms the anode and the aluminum can the cathode. The counter operates on argon gas admixed with 2.5% carbon dioxide or methane to make the gas multiplication less sensitive to small changes in the anode voltage. The proportional counter is of the continuous flow type. This insured a constancy of the gas pressure which is essential to keep the gas multiplication constant. Typical operating pressures are between 6 and 7 cm of Hg and the anode voltage is between 500 and 600 volts.

The reaction products enter the proportional counter through a thin aluminized Mylar window (0.65 mg/cm^2) on a side of the box. A 1.5 mm deep surface barrier detector is mounted directly opposite the window inside a region of the body of the proportional counter that is electrically isolated from the active volume by a thin (1000 Å) nickel foil (see Figure 3). This protects the surface barrier detector against any accidental breakdown of the proportional counter high voltage through the counter. Housing the surface barrier detector in the argon atmosphere solved a second problem in addition to eliminating an exit window for the δE-counter. This had to do with the

electrical breakdown of the surface barrier counter's bias voltage (~ 180 volts) along its surface in a pure helium atmosphere.

The reaction products pass through the Mylar and nickel foils, the target and proportional counter gases before reaching the solid state detector. This matter stops protons and alpha particles with energies less than about 0.6 and 2.0 MeV, respectively. Higher energy particles merely loose some fraction of their initial energy. This limits the energy spectra on the low energy side to about 600 keV for protons and about 2 MeV for alpha particles. Further, the spectra as measured by the thick counter are distorted by the energy loss. This distortion can easily be corrected, from a knowledge of the energy loss data, as described in the next chapter.

The entire proportional counter assembly, with the solid state counter mounted inside it, can be rotated about the center of the target chamber, the most backward angle accessible being 140^{o}. For counter angles more forward than 45^{o}, the proportional counter body eclipsed the incident beam and obscured the calorimeter thus limiting absolute differential cross section measurements to the range of angles 45^{o} - 140^{o}. For more forward angles, a monitor counter fixed at an angle of 90^{o} to the beam was used.

The absolute angle setting accuracy is correct to within $\pm 2^{o}$.

E. Counter Geometry

Gas targets do not have a well defined thickness as do thin solid targets. Rather, the thickness of the gas target used for measurements has to be defined by a slit in addition to the aperture immediately in front of the detector which defines the solid angle

subtended. It is important that the beam length so defined be completely enclosed in the available beam length at all angles studied, i. e., no part of the canal should come into the view of the detector.

The slit system consists of a circular aperture of radius a ($\sim$ 5. 5 mm) placed immediately in front of the solid state detector. This is at a distance D ($\approx$ 80. 5 mm) from the center of the target chamber. The second slit is rectangular with its length much greater than its width, 2W. This slit is placed symmetrically about the line joining the center of the target chamber and the center of the circular aperture in front of the surface barrier counter. The length of the slit is placed perpendicular to the reaction plane as shown in Figure 4. The distance between this slit and the circular aperture is d($\approx$ 67. 5 mm). The quantities a, W, D and d define the geometrical factor. Different counter geometries were employed by varying W. (Parameters for the defining slit and aperture are listed in Table 1 for the various geometries employed.)

The solid angle subtended by the counter varies from point to point along the length of the beam defined by the slit system as shown in Figure 5C. The geometrical factor that enters the formula for the reaction yield is $\int_{-\beta}^{\beta} \Omega(\zeta)d\zeta$ where ζ is the co-ordinate along the path of the beam, measured from the center of the target. $\Omega(\zeta)$ is the solid angle subtended by the counter at the co-ordinate value ζ. $\pm \beta$ are the extreme values of ζ seen by the detector (see Figure 5A). This quantity has been calculated for a line beam (i. e., neglecting the finite size of the beam) and for the detector at 90^{o} to the beam direction in Appendix 3. There it is shown that

$$\langle \Omega \ell \rangle_{90^o} = \frac{(\pi a^2) \cdot 2W}{D \cdot d} \left[1 - \frac{W^2}{2d^2} - \frac{3a^2}{8D^2} - \frac{3a^2}{8d^2} + O\left(\left\{\frac{W + a}{D}\right\}^4\right) \right] .$$

For any other detector angle,

$$\langle \Omega \ell \rangle_{\psi} \approx \langle \Omega \ell \rangle_{90^o} \csc \psi .$$

III. EXPERIMENTAL PROCEDURE

A. Particle Spectra

The outgoing particle spectra were measured by a counter telescope consisting of the gas proportional counter described in Section II. D. and a thick ($\sim$ 1500 μ) surface barrier solid state detector. The latter was not only sufficiently thick to stop the most energetic protons observed in the $^3He + {}^3He$ reaction, but also was able to stop the protons from the $d(^3He, p)^4He$ reaction. Signals from the two detectors fed two low noise charge sensitive preamplifiers. The preamplifier pulses were amplified by double delay line pulse amplifiers and fed to a 'Nuclear Data' two dimensional pulse-height analyzer operating in a 64 x 64 channel mode. The analyzer was gated with a signal from the solid state counter (E') to reject δE pulses from the proportional counter that were unaccompanied by an energy signal from the surface barrier device. A block diagram of the electronics is shown in Figure 8. An E'-pulse was always accompanied by a δE-signal since the solid angle subtended by the surface barrier detector is completely enclosed inside the solid angle of the proportional counter. The anode wire of the proportional counter is positioned such as not to eclipse any part of the solid state counter.

The timing of the gate pulse had to be carefully set to insure that no genuine events were lost. The timing was set with pulses from a pulser feeding both preamplifiers. The delay of the coincidence gate signal was slowly varied until the events just ceased to be recorded for two extreme delay settings. The delay was then set half way between these limits.

The particle spectra were shown on the CRT display of the analyzer as two nearly rectangular hyperbolas well separated from each other and from any background. One such display is shown in Figure 9. The two tracks in the δE-E' plane are associated with protons and alpha particles. Raw particle spectra are obtained by summing all the counts in various δE-channels corresponding to a definite E'-channel about the locus of a particular hyperbola.

Correction of raw spectra - The particle spectra as measured by the analyzer are distorted due to the energy loss in passing through matter before reaching the thick counter. The true spectrum of the emitted particles is calculated in the following way.

From energy loss data [Whaling, 1958], proton and alpha particle energies are calculated at the position of the detector as a function of their initial energies, i.e., at the center of the target chamber. There is a one-to-one correspondence between the energy E at the target and the energy E' at the solid state (E') counter for each type of particle. From a plot of E' vs E, the slopes $\frac{dE'}{dE}\Big|_{E'}$ are calculated for various E'. The true spectrum N(E)dE is obtained from the observed energy spectrum N(E')dE' by the relation

$$N(E)\,dE = \left\{ N(E') \frac{dE'}{dE}\Big|_{E'} \right\} dE \quad .$$

Proton spectra and total yields - Proton spectra were obtained by setting the δE-pulse gain higher by a factor of four than that used for obtaining the alpha spectra, to raise the proton track

from the abscissa (E'-axis) but then the alpha particles were out of the range of the analyzer. The measured proton spectra extend from the three-body end point down to about 600 keV. Protons starting with energies less than 600 keV are stopped in the matter between the target region and the surface barrier detector.

At very low energies ($E_{^3He}$ < 200 keV) the shape of the proton spectra is nearly that given by a statistical distribution. At higher energies the spectra begin to exhibit effects of final-state interactions which get stronger with increasing energy. The effect of final-state interaction between a proton and ^4He shows up in the proton spectra as a sharp peak in the spectrum corresponding to the two-body breakup: ^5Li + p and a rather broad peak corresponding to the subsequent decay of ^5Li in flight. Suggestions of a small peak related to ^5Li + p exist even in the lowest energy spectrum at $E_{^3He}$ = 0.19 MeV (see Figure 14).

Total proton yields are obtained by summing all the counts in the various energy intervals of the observed spectrum. A correction is made for that part of the spectrum not observed (energy < 600 keV) by assuming that the spectral shape in this range of energies is given by phase space alone. This assumption, though not valid for all energies studied, gives, however, a crude estimate for the number of protons not observed. Since only a small fraction of the entire spectrum is being accounted for, the error introduced by this assumption is expected to be small.

Proton spectra at several energies and at 90° to the beam direction are shown in Figures 10 to 14.

B. Proton Angular Distributions

Proton spectra have been obtained at several angles in the range of 20^{o} - 140^{o} for seven energies. Figure 15 shows proton spectra at 25^{o} and 140^{o} in the laboratory for a bombarding energy of 300 keV. The general shape of the spectrum is not sensitive to the angle of observation.

Total proton yields were obtained at each angle by the method described above. Several methods were used to normalize the proton yields at different angles for the same energy. Also, the angular effects introduced by the variation of the geometrical factor with the angle were taken out.

Angular distributions have been obtained at helium-3 energies of 2.0, 1.0, 0.75, 0.60, 0.50 and 0.30 MeV. The measurements at 2.0, 1.5, 1.0, 0.6 and 0.5 MeV were made with the aid of a monitor counter set at an angle of approximately 45^{o} to the incident beam, to observe the elastically scattered ^{3}He. At these energies, only relative angular distributions were obtained using the monitor counter. Total cross sections were determined from the relative angular distributions and the measured absolute differential cross section at 90^{o} to the beam. The relative angular distributions at 2.0, 1.5 and 1.0 MeV are shown in Figures 16 and 17.

Angular distributions at 0.743 and 0.300 MeV were measured using a monitor counter set at 90^{o} to the incident beam direction. This counter was placed outside the target chamber behind a thin Havar window as shown in Figure 1. The window stopped both the ^{3}He's and the alpha particles but passed the high energy protons. The detector was suitably collimated and was set

up to observe the high energy protons from the reaction studied. All protons with energies in excess of a certain threshold were counted. Protons from the $d(^3He, p)^4He$ reaction were unimportant. In addition to the monitor counter, the beam integrator was also used over the range of 45^o - 140^o. At more forward angles ($< 45^o$) the proportional counter body interfered with the beam and hence only the monitor was employed for normalization. Measurements with the beam integrator gave directly the differential cross sections while the measurements with the monitor counter yielded only the relative angular distributions. The relative angular distributions were normalized to the absolute differential cross sections by determining the proportionality factor by a least squares fit to data obtained with both the monitor counter and the beam integration device. Proton angular distributions at these energies are shown in Figure 18.

C. Alpha Particle Spectra

Alpha particle spectra have been obtained at several angles for several bombarding energies. The measured alpha spectra extend from the three-body end point down to about 2 MeV. The raw alpha spectra are much more distorted than the proton spectra due to the larger energy loss. The alpha spectra are corrected in the same manner as the proton spectra but the corrected spectra are less reliable because of the higher energy loss and faster change in the energy loss with energy. Figures 19 and 20 show three α-spectra at helium-3 energies of 1.5, 1.0 and 0.75 MeV in the forward direction.

D. Differential Cross Sections - Laboratory System

For a gas target and a line beam, the total proton yield at 90^{o} to direction of the incident beam is given by

$$Y = 2N_B n_T \int_{-\beta}^{+\beta} d\zeta \int_{-a}^{P} dx \int_{0}^{\sqrt{a^2-x^2}} \frac{2D\, dy}{[(\zeta-x)^2+y^2+D^2]^{3/2}} \cdot \left.\frac{d\sigma}{d\Omega}\right|_{(E(\zeta),\, \psi(x,y,\zeta))}$$

where Y = the total proton yield

N_B = the number of ^{3}He ions (from the beam)

n_T = the density of target nuclei in the target region

$\left.\frac{d\sigma}{d\Omega}\right|_{E,\psi}$ = the differential cross section in the laboratory at energy E and angle ψ.

The remaining quantities have the same meaning as defined in Appendix 3.

$$\Omega(\zeta) = \int_{-a}^{P} dx \int_{0}^{\sqrt{a^2-x^2}} \frac{2D\, dy}{[(\zeta-x)^2+y^2+D^2]}$$ is the solid angle subtended by the counter at a point along the beam path, defined by the co-ordinate ζ.

The energy varies along the beam path due to energy loss, thus

$$E = E(\zeta).$$

The angle ψ varies from point to point along the beam path and also from point to point of the detector where the reaction product enters

$$\psi = \psi(x, y, \zeta) .$$

Finally, the factor 2 appears in the formula for the yield because two protons are released per reaction.

Approximations

1. Since the angular distributions exhibit only weak angular dependence of the differential cross section, the variation of the cross section over the range of angles encountered at a mean angle setting can be ignored.

2. As the energy loss over the total length of the beam observed is small, the energy loss can be regarded as linear in ζ, i. e.,

$$E(\zeta) = E_0 - \epsilon\zeta$$

where E_0 is the energy at the center of the target and ϵ is the specific energy loss at energy E_0 and the appropriate gas pressure.

Over this small range of energies, we can further assume

$$\frac{d\sigma}{d\Omega} \alpha \frac{1}{E} e^{-\frac{\alpha}{\sqrt{E}}} \qquad \text{where} \qquad \alpha = 2\pi\eta\sqrt{E}$$

$$\text{Then } \frac{d\sigma}{d\Omega}(E(\zeta)) \approx \frac{d\sigma}{d\Omega}(E_0)\left[1 - \frac{\epsilon}{E_0}\left(\frac{\alpha}{2\sqrt{E_0}} - 1\right)\zeta + \frac{\epsilon^2}{E_0^2}\left(\frac{\alpha^2}{8E_0} - \frac{7}{8}\frac{\alpha}{\sqrt{E_0}} + 1\right)\zeta^2\right].$$

With these approximations, one gets

$$Y = 2N_B n_T \left.\frac{d\sigma}{d\Omega}\right|_{E_0} \int_{-\beta}^{\beta} \left[1 - \frac{\epsilon}{E_0}\left(\frac{\alpha}{2\sqrt{E_0}} - 1\right)\zeta + \frac{\epsilon^2}{E_0^2}\left(\frac{\alpha^2}{8E_0} - \frac{7}{8}\frac{\alpha}{\sqrt{E_0}} + 1\right)\zeta^2\right]\Omega(\zeta)d\zeta$$

Since $\Omega(\zeta)$ is an even function of ζ, $\int_{-\beta}^{\beta} \Omega(\zeta)\,\zeta d\zeta$ vanishes.

3. To carry out the second order integral, a trapezoidal approximation is made for the shape of $\Omega(\zeta)$. In this approximation

$$\Omega(\zeta) = \Omega_0 \quad \text{for} \quad |\zeta| < \alpha$$

$$\Omega(\zeta) = \Omega_0 \frac{(\beta - \zeta)}{(\beta - \alpha)} \quad \text{for} \quad \alpha < |\zeta| < \beta$$

where α and β are defined in Appendix 3. On carrying out the integration one obtains for the total proton yield at 90^o in the laboratory

$$Y \approx 2N_B n_T \left.\frac{d\sigma}{d\Omega}\right|_{(E_0, 90^o)} \times \left[1 + \frac{\epsilon^2}{E_0^2}\left(\frac{\alpha^2}{8E_0} - \frac{7}{8}\frac{\alpha}{\sqrt{E_0}} + 1\right)\left(\frac{D^2W^2 + a^2(D-d)^2}{3d^2}\right)\right]$$

$$\times \langle \Omega \ell \rangle_{90^o} .$$

Energy spread - The foregoing has been obtained with the assumption that the beam energy is sharply defined at each point along the target region. However, there is a spread in the beam energy due to the inherent energy spread in the primary beam, the energy straggle in passing through the target gas and effects due to any non-uniform radial pressure distribution in the canal. Again for a symmetric energy distribution about the mean, the first order correction is zero. The second order term is calculated for a Gaussian shape $\left[e^{-\frac{(E - E_0)^2}{2\Delta^2}} \right]$ for the energy distribution. With this correction included, the reaction yield is given by

$$Y \approx 2N_B n_T \left.\frac{d\sigma}{d\Omega}\right|_{(E_0, 90^o)} \left[1 + \frac{1}{E_0^2}\left(\frac{\alpha^2}{8E_0} - \frac{7}{8}\frac{\alpha}{\sqrt{E_0}} + 1\right) \times \left(\frac{\epsilon^2}{3d^2}\left[D^2W^2 + a^2(D - d)^2\right] + \Delta^2\right)\right] \langle \Omega \ell \rangle_{90^o} .$$

Finally, inserting the value of $\langle \Omega \ell \rangle_{90^o}$ from Appendix 3, one obtains for the total proton yield at 90^o

$$Y \approx 2N_B n_T \left.\frac{d\sigma}{d\Omega}\right|_{(E_0, 90^o)} \cdot \frac{\pi a^2 (2W)}{D \cdot d} \left[1 + \frac{1}{E_0^2}\left(\frac{\alpha^2}{8E_0^2} - \frac{7}{8}\frac{\alpha}{\sqrt{E_0}} + 1\right) \times \left(\frac{\epsilon^2}{3d^2}\left[D^2W^2 + a^2(D - d)^2\right] + \Delta^2\right) - \frac{W^2}{2d^2} - \frac{3a^2}{8D^2} - \frac{3a^2}{8d^2}\right] .$$

The correction terms are really very small under the circumstances of the present experiment. The second order term has been explicitely calculated to point out the probable errors and to estimate them rather than to provide a more accurate value of the cross section. It suffices to use the following formula for calculating the cross section

$$\left.\frac{d\sigma}{d\Omega}\right|_{(E_0,\,90^o)} \approx \frac{Y}{2N_B n_T \left\{ \frac{(\pi a^2)2W}{D\cdot d} \right\}} \cdot$$

Other angles - At angles other than 90^o, the cross section factor is calculated similarly except that the geometrical factor $\langle \Omega \ell \rangle$ at a laboratory angle ψ is given by

$$\langle \Omega \ell \rangle_\psi \approx \langle \Omega \ell \rangle_{90^o} \csc \psi \ .$$

In this case $\Omega(\zeta)$ is not entirely symmetric with respect to ζ. This introduces small non-vanishing first order corrections.

E. Total Reaction Cross Sections

The total reaction cross sections are obtained by a simple numerical integration of the measured angular distributions. These are compared with $4\pi\sigma(90^o)$ where $\sigma(90^o)$ is the differential cross section at 90^o in the laboratory. The two quantities differ by 8% at 2 MeV and only by 1% at 300 keV bombarding energy, the total cross section σ being always larger than $4\pi\,\sigma(90^o)$. The ratio of σ to

$4\pi\sigma(90^{o})$ is very smooth when plotted as a function of the energy and approaches unity as the energy approaches zero. At energies where no angular distributions have been obtained the total cross section is obtained from $4\pi\sigma(90^{o})$ and the interpolated ratio $[\sigma/4\pi\sigma(90^{o})]$. The energy dependence of the total cross section is shown in Figure 21. The total reaction cross sections are tabulated together with the errors in the measurement in Table 3.

F. The Cross Section Factor

The cross section factor is calculated from the total cross section with the aid of the defining formula:

$$S(E_{cm}) = \sigma(E_{cm}) \cdot E_{cm} \cdot \exp(2\pi\eta) \quad \text{where} \quad \eta = \frac{z_1 z_2 (e^2/\hbar c)}{\sqrt{E_{cm}}} \times \sqrt{\frac{\mu c^2}{2}}$$

$$S(E_{cm}) = \sigma(E_{cm}) \cdot E_{cm} \cdot \exp\left(\frac{4.8595}{\sqrt{E_{cm}}}\right) \rightarrow (E_{cm} \text{ in MeV}) .$$

E_{cm} is the center-of-mass energy which is taken as one half the energy at the center of the target. $\sigma(E_{cm})$ is the total cross section at the center-of-mass energy, E_{cm}.

The cross section factor has been obtained at several energies from 1.1 MeV to 80 keV in the center-of-mass system. The cross section factors are tabulated in Table 4 and a plot of S(E) vs E is shown in Figure 23. The experimental points have been fitted to the function

$$S(E) = S_0 + S_1 E \text{ , where } E = E_{cm}$$

over different ranges of energies. The coefficients S_0 and S_1 have the following values:

1. $S_0 = (5.3\ ^{+0.9}_{-0.7})$ MeV-barns; $S_1 = (-3.7 \pm 3.4)$ barns for $E_{cm} < 200$ keV.

2. $S_0 = (5.0\ ^{+0.65}_{-0.45})$ MeV-barns; $S_1 = (-2.1 \pm 1.1)$ barns for $E_{cm} < 350$ keV.

3. $S_0 = (5.0\ ^{+0.6}_{-0.4})$ MeV-barns; $S_1 = (-1.8 \pm 0.5)$ barns for $E_{cm} < 500$ keV.

It was necessary to include a quadratic term in energy to obtain a fit to the experimental data over the entire range of energies. That is, the function $S(E) = S_0 + S_1E + S_2E^2$ was used to obtain the fit. The following values for the coefficients were obtained:

$$S_0 = (5.1 \pm {}^{0.6}_{0.4})\ \text{MeV-barns},\ S_1 = (-2.6 \pm 0.85)\ \text{barns}$$

$$\text{and}\ S_2 = (1.1 \pm 0.65)\ \text{barns/MeV}.$$

This fit was made to obtain an analytical expression for the cross section factor which is valid over a larger range of energies and not for extrapolation of the cross section factor to lower energies.

G. The $^{3}He(d, p)^{4}He$ Reaction

Differential cross sections at 90^{o} in the laboratory have been measured for the above reaction with the same techniques used for the $^{3}He + ^{3}He$ measurements. Both ^{3}He and deuteron beams were employed with the appropriate choice of the target. With deuterium target the gas could not be cleaned by the zeolite trap. Instead, the trap was by-passed using the by-pass line [see Figure 2] but the gas was frequently changed to keep the level of contaminants low. A graph of the differential cross section at 90^{o} in the laboratory as a function of the energy is shown in Figure 22.

The accuracy of these measurements are somewhat better than for the $^{3}He + ^{3}He$ measurements. The gross errors in the differential cross sections are estimated to be (+10%, -7%). These results are in very good agreement with the measurements of Yarnell et al. (1953) who quote a much larger error for their measurements.

IV. DISCUSSION OF ERRORS

The errors in the determination of the cross section factor, S(E) arise from the errors in the measurement of the total cross section $\sigma(E)$ at an energy E and from the uncertainties in the knowledge of the energy E itself. The errors can be further classified into two categories - systematic and statistical. Often this distinction is not sharp and even the errors quoted do not have a precise meaning because of the subjective nature of assessing some of the errors involved.

A. Errors in the Measured Values of the Total Cross Sections

The total error in the measured value of $\sigma(E)$ is contributed by errors in the quantities N_B, n_T, Y, $\langle \Omega \ell \rangle$ and by the approximations made in the formula used for calculating the cross section. This last quantity is very small compared to the other uncertainties and hence can be neglected.

Error in N_B - In the present method of beam integration, the number N_B is obtained as the ratio of the total beam energy deposited in the calorimeter to the energy of each of the ^{3}He nuclei at the beam stopper. Each of these two quantities have associated uncertainties.

The error in the total beam energy deposited in the calorimeter can be made small ($< \pm 4\%$) by making the calibration of the beam integration device under conditions as nearly identical as possible with that of the experiment. This is best achieved by making calibrations immediately preceeding and following the

experimental run. This error is regarded as mainly statistical in nature. Systematic errors due to the different conditions of calibration and experimental runs are believed to be small.

The uncertainty in the beam energy at the integrator is due to the lack of accurate energy loss data. The specific energy loss reaches a maximum at about 400 keV. Typical energy losses near this energy are about 100 keV. An uncertainty in this quantity of ± 15% results in an uncertainty of ± 5% in the energy at the integrator. At lower energies these errors could become very serious but the situation actually improves because of the decrease in energy loss with energy and because more accurate information on energy losses are available [Weyl - quoted in Whaling, 1958]. This is clearly a systematic error, but when several measurements are made with different target pressures the changes in the systematic error contributes a statistical component to the errors.

The total error in N_B is adopted as ± 6%.

Error in n_T - n_T is a function of the pressure, temperature and the extent of impurities. The only impurity to be concerned with is helium-4. The ^{3}He used was supplied by Mound Laboratory, Miamisburg, Ohio; who quote an impurity level of 0.43% for ^{4}He. From observations of the proton elastic scattering from the target, the impurity level of heavier atoms ($A > 3$) is known to be less than 1%.

Pressure measurements could be made with an accuracy of 0.1 mm or 2%, whichever is higher. There is some uncertainty in the pressure profile in the vicinity of the canal. Most violent pressure (and density) gradients occur within one diameter (of the canal) from the tip of the canal. Effects reaching out to the center

of the target are considered to be less than a few percent. The temperature of the gas in the wake of the beam is not expected to be significantly different from the average temperature of the gas in the chamber. This was ascertained by observing the reaction at a fixed energy with widely different beam currents. No systematic dependence of the total cross section with the beam current was observed.

The error in n_T is entirely systematic; further, the error is mainly in the direction of lower n_T. The cumulative error is taken as -5%, +2%.

Error in Y - The error introduced in Y due to counting statistics, dead time of analyzer and background subtraction is less than ±3% except for measurements at $E_{^3He} < 300$ keV where counting statistics are poorer. The other source of error is in estimating the number of low energy protons unobserved. This is certainly less than ±3% since the fraction of the spectrum not observed constitutes only 5-6%.

Error in $\langle \Omega \ell \rangle$ - This stems from the approximations made in the calculation of $\langle \Omega \ell \rangle$, the alignment of the slit system and the errors associated with the measurement of dimensions and distances. This error is estimated with a good degree of precision to be ±3%.

The cumulative error in $Y/N_B n_T \langle \Omega \ell \rangle$ is +13%, -9%. This assignment seems conservative in the light of elastic scattering measurements of protons from argon-40. The measured cross sections are compared with the Rutherford values in Table 2. The error is generally in the direction of smaller measured cross sections except at the higher energies ($E_p > 1$ MeV). The $^{40}A(p, p)^{40}A$

measurements indicate an error considerably less than 9% but this is to be expected because of the more favorable conditions of the elastic scattering measurements. The error assignment is quite consistent with the deviations observed in the proton elastic scattering from argon-40.

There is one other source of error contributing to the total cross section measurements which has to do with the integration of the differential cross section. This error is entirely negligible. Thus the errors assigned to the individual measurements of the total cross sections are +13%, -9%.

B. Error in the Knowledge of Energy, E

The energy calibration of the magnetic analyzer is known to within ± 1 keV. The energy loss suffered by the primary beam before reaching the center of the target has associated with it errors due to the uncertainty in the specific energy loss and due to the uncertainty in the effective thickness of the canal. The density of the gas inside the canal is nearly 0.6 times the density in the target chamber. However, this number gets modified due to the roughness of the inside of the canal and the shaping of the entrance to the canal, etc.. The energy loss in reaching the center of the chamber is always less than 16 keV. The total uncertainty in this is estimated at ± 3 keV. Again this error is somewhat smaller at the lower energies due to the smaller specific energy loss and due to the availability of more accurate energy loss data [Weyl - quoted in Whaling, 1958]. This is rather fortunate as the cross section factor is very sensitive to the energy at very low

energies. The errors introduced into N_B and E by uncertainties in the specific energy loss contribute to errors in the cross section factor in opposite directions. There is therefore a partial compensation of the systematic error introduced by the error in the specific energy loss.

The error in the knowledge of the energy at the center of the target is therefore about ± 2.5 keV. This error is systematic.

Energy spread - The beam energy has a finite energy spread when it emerges from the analyzer. Further spreading of energy occurs due to the statistical value of the energy loss process. Any non-uniform radial density distribution in the canal produces another type of energy spread. These quantities are all small, a virtue of the differentially pumped system. The percentage full width at half maximum reaches a maximum at the lowest energy. It is only 2.5% at the lowest energy investigated. Since the energy spread gives rise to corrections of only the second order, this correction is unimportant and the errors are small.

The errors described above are only the gross features. The errors vary from measurement to measurement due to changes in energy, target pressure counting statistics, etc.. But these changes are quite small except at very low energies where both counting statistics and energy terms contribute large errors. The total error associated with individual S(E) measurements is tabulated with the values of the cross section factors in Table 4.

The various factors contributing to the error are summarized in Table 5. Quite often relative errors have been assigned to quantities which prima facie have only systematic errors. This is due to changes in the experimental set up. For instance, several

different geometries have been employed, two different beam integrating devices have been used and the target pressure has been varied over a wide range of pressures. Thus the geometrical factor, the number N_B of incident ^3He and the energy losses which have mainly systematic errors associated with them, contribute different systematic errors when the experimental conditions differ. These changes in the systematic errors have been absorbed as a relative error. This is a possible method to reduce systematic errors at the cost of relative errors. These relative errors are minimized by repeated measurements with different experimental conditions.

C. Errors in S_0 and S_1

The measured cross section factors S(E) are fitted to the function

$$S(E) = S_0 + S_1 E$$

of energy by a standard least squares routine. The data points are weighted according to the inverse square of their statistical errors. The resulting S_0 and S_1 have errors. The error in S_0 is much smaller than the errors in the individual S(E) because of the large number of data points. However, the error in S_1 is not ameliorated. To these errors, the systematic errors have to be added. The systematic errors (+10%, -7%) affect only the S_0 and not S_1. The errors are compounded in the usual way. The errors in S_0 and S_1 for fits over three different ranges of energy are given in Table 6.

V. DISCUSSION

A. Comparison of Results

The total reaction cross section for the reaction under investigation was first measured by Good et al. (1953) over the range of bombarding energies between 100 and 800 keV. The present investigation was undertaken since their results were considered to have large errors. Since starting on this project, measurements of total cross section for this reaction have been reported by Neng-Ming et al. (1966). The work of Neng-Ming et al., covers the energy range $E_{^3He}$ = 500-1700 keV. Also Bacher and Tombrello (1967) have extended their measurements on this reaction to very low energies. It is the purpose of this section to compare the results of this study with the results of the other groups. The cross section factor, S(E) rather than the total cross section will be the quantity used for comparing the results. This has the advantage of lumping all the errors into one quantity.

This investigation yields a cross section factor that is only slowly varying in energy. The zero energy cross section factor obtained has the value

$$S_0 = \left\{ 5.0 \begin{matrix} +0.6 \\ -0.4 \end{matrix} \right\} \text{ MeV-barns} .$$

The results of Good et al. are in serious disagreement with the present work. Their cross section factor decreases rapidly from a value S = 2.4 MeV-barns at $E_{^3He}$ = 600 keV to

1.2 MeV-barns at 300 keV. Below this energy the cross section factor increases sharply. This discrepancy is attributed to the incomplete information on the distribution of ^{3}He in their target and the uncertainty in the energy losses for ^{3}He in their target material.

The measurements of Neng-Ming et al. are in general agreement with the measurements reported here. The values of S(E) agree within the combined errors of the two measurements, their S(E) being systematically lower. Their measurements seem to indicate an even slower variation of S(E) with energy than observed here, but they quote much larger errors in their energy determination, which is reflected in the cross section factor.

Bacher and Tombrello have measured the total cross sections at energies as low as 304 keV with apparatus similar to that used for the higher energy measurements. They minimized the uncertainty in energy by carefully determining the energy loss in the entrance window at precisely the experimental energies. Their results are in very good agreement with the results obtained in this study. The absolute S(E) agree within the limits of the combined errors, with their values being systematically higher by about 8%. Particularly impressive is the agreement in the variation of S(E) with energy. The small systematic difference in the absolute values of S(E) is not serious considering that the measurements were made by two very different methods.

The results of these three groups are compared with the results of the present work in Figure 22.

B. Nuclear Physics of the Reaction

Bacher and Tombrello (1965) have investigated this reaction in detail for ^{3}He energies between 1.0 and 20.0 MeV. The process has been understood by them as proceeding mainly through the intermediate state of (^{5}Li + p) for energies greater than 3 MeV. Excellent fits to the proton spectra have been obtained according to this model. However, at energies below 3 MeV the above model is not entirely adequate. The trend observed by Bacher and Tombrello in the change in shape of the proton spectra with decreasing energy has been observed to continue the same pattern in this study. While at energies > 3 MeV, the process is explained as entirely sequential, the proton spectrum at $E_{^{3}He}$ = 0.19 MeV [Figure 14] shows very little evidence of the two step process. It seems therefore, a second process is dominant at very low energies. May and Clayton (1968) have considered the possibility of the reaction proceeding by a 'neutron tunnelling' mechanism. In this process, a neutron is considered to 'tunnel' from one ^{3}He to the other even when the two nuclei are relatively far apart. At incident energies well below the Coulomb barrier, this mechanism could dominate other processes which require deeper penetration of the Coulomb barrier. This would explain the change in the shape of the proton spectra because the 'neutron tunnelling' mechanism may enhance a final state interaction in the 2p system rather than the (^{4}He + p) system.

The cross section factor - May and Clayton calculate the cross section factor for the reaction on the basis of this model. They regard the di-proton as a particle that lives long enough to

leave the region contributing most to the nuclear matrix elements. They consider pure Coulomb waves for the scattering states and zero range potentials for the interaction. On the basis of these assumptions, they calculate the cross section factor as a function of the bombarding energy. Several variations are made on their basic model by different choices for the neutron wave function in the ^{3}He and ^{4}He. They calculate a negative value for the slope of S(E) as observed experimentally, but the value of the calculated slope is much less than the slope required to fit the data. Furthermore, for a realistic comparison of the calculations with the experiment, the contribution to the total cross section from the (^{5}Li + p) mechanism will have to be subtracted from the measured total cross sections because the calculations of May and Clayton consider only "neutron transfer" process. While there is no clear way of subtracting from the experimental data, the contribution from the sequential process, it is clear that however this contribution is removed, the effect will be to make the slope of S(E) a larger negative quantity, making the disagreement with the theory even more serious.

To fit the experimental data, the total cross section for reaction between nuclei of type i and type j is written as

$$\sigma_{ij}(E) = \frac{(1 + \delta_{ij})}{2} \frac{\Sigma'(E)}{\sqrt{E}} \rho_f \left[\sum_L W_L \int_0^\infty P_L(R)\, T_L(R) dR \right]$$

where $\sigma_{ij}(E)$ is the total reaction cross section at energy E. The first term on the right hand side is due to identical particles, normalized to 1 for interaction between like particles. $\Sigma'(E)$ is analogous to S(E) and ρ_f is the density of final states. The $1/\sqrt{E}$ is the usual flux term. W_L, $P_L(R)$ and $T_L(R)$ are the statistical weights, the probabilites of finding the two interacting nuclei at a separation R and the probability that a rearrangement will occur when they are so separated. The subscript L refers to the angular momentum of the partial wave considered.

Rather than to calculate the integrals, they are parametrized by writing

$$\int_0^\infty P_L(R)\, T_L(R)\, dR = P_L(R_L) = \frac{1}{F_L^2(KR_L) + G_L^2(KR_L)}$$

where R_L are parameters adjusted to fit the data, and F_L and G_L are the regular and irregular Coulomb functions. The different radius parameters for different partial waves effectively take into account different strengths for these waves. Further simplification is obtained by regarding ρ_f to be constant because of the large Q value for the reaction. Then,

$$\sigma_{ij}(E) = \frac{(1 + \delta_{ij})}{2} \frac{\Sigma(E)}{\sqrt{E}} \left[\sum_L W_L P_L(R_L) \right]$$

where

$$\Sigma(E) = \rho_f \Sigma'(E) \ .$$

For the $^3He + {}^3He \rightarrow {}^4He + 2p$ reaction, both S and P-waves were regarded important because of the large statistical weight for P-waves.

$$\sigma(E) = \frac{\Sigma(E)}{\sqrt{E}} \left[P_0(R_0) + 9P_1(R_1)\right]$$

$$\Sigma(E) = \sigma(E)\sqrt{E}\left[\frac{1}{P_0(R_0) + 9P_1(R_1)}\right].$$

The radius parameters R_0 and R_1 were adjusted to make $\Sigma(E)$ very nearly independent of energy. The fits are not very sensitive to small changes in R_0 and R_1. A best fit was obtained for $R_0 = 3.7$ fm and $R_1 = 3.0$ fm. The values of $\Sigma(E)$ as a function of the energy E is shown in Figure 24. The nearly constant value of $\Sigma(E)$ is ~ 0.027 $MeV^{1/2}$-barns.

The same parameters have been used to fit the total cross section data on the mirror reaction $T + T \rightarrow {}^4He + 2n$ investigated by Jarmie and Allen (1958) and by Govorov et al. (1962). A reasonable fit is obtained and the nearly constant value of $\Sigma(E)$ for this reaction [$\Sigma(E) \sim 0.03$ $MeV^{1/2}$-barns] is very nearly equal to the $\Sigma(0)$ obtained for the $^3He + {}^3He$ reaction.

It was then considered to fit the $^3He + T$ data of Youn et al. (1961) using the same radius parameters. However, in this case the statistical weights are different due to the possibility of having both singlet and triplet spin states for a given relative angular momentum in the incident channel.

$$\text{For } T + {}^3\text{He}, \ \sigma(E) = \frac{1}{2} \frac{\Sigma(E)}{\sqrt{E}} [4 P_0(R_0) + 12 P_1(R_1)]$$

$$\text{or } \Sigma(E) = \sigma(E) \sqrt{E} [2 P_0(R_0) + 6 P_1(R_1)] \ .$$

The existence of the bound state in the (np) system complicates the situation further. For this reason the (^{3}He + T) total reaction cross sections and the partial cross sections for ^{3}He + T $\rightarrow$ ^{4}He + n + p are separately fitted with the same radius parameters; R_0 = 3.7 fm and R_1 = 3.0 fm. These fits are shown in Figure 25 together with the fit for the T + T reaction. It is remarkable that these three reactions should yield values of $\Sigma(0)$ which agree within a factor of about 2.

C. Astrophysical Significance

The termination of the proton-proton chain has remained uncertain ever since it was considered as an important source of energy in stars, by Bethe and Critchfield (1938). At that time there was some uncertainty in the stability of ^{3}He against β-emission. However, the ^{3}He$(\alpha, \gamma)^7$Be$(e^-, \nu)^7$Li$(p,\alpha)^4$He mode was regarded as the possible termination. The ^{3}He + ^{3}He $\rightarrow$ ^{4}He + 2p mode was suggested by C. C. Lauritsen [Fowler, 1951] and by Schatzman (1951) as the most probable termination. Subsequent measurements of the reaction cross section for ^{7}Li$(p, \alpha)^4$He reinstated the ^{3}He + ^{4}He mode as competing with the ^{3}He + ^{3}He termination. Study of the ^{8}B nucleus opened another possible termination viz. ^{3}He$(\alpha, \gamma)^7$Be(p, γ) ^{8}B$(e^+ \nu)^8$Be$(\alpha)^4$He.

Now it is reasonably certain that only these three processes are important. But then, the branching ratios for the three terminations have been in doubt. This has been attributed to the uncertainty in the reaction cross section for the $^3He(^3He, 2p)^4He$ reaction. The results of the present investigation show that the cross section factor for this reaction is a factor of 4.5 larger than the value adopted from the measurements of Good et al. (1953).

Such a change in the value of the cross section factor for this reaction, can in principle, change the model of the Sun drastically. This is because a termination of the chain through the $^3He + ^3He$ mode requires two primary weak processes to effectively fuse four protons into a helium-4 while a termination through either of the other two processes require only one primary reaction to achieve fusion of four protons into an α-particle. In the later process, the existing ^4He acts as a catalyst while the first process proceeds acatalytically. Since the slowest reaction in a chain determines the overall rate, the (p + p) process determines the rate of energy production. Thus the central temperature and other characteristics of the Sun could depend strongly on the cross section factors for the $^3He + ^3He$ and $^3He + ^4He$ processes. But the changes caused by this difference on the solar model are rather restrictive. With the accepted value of the cross section factor for the $^3He(^4He, \gamma)^7Be$ reaction, most of the energy generation occurs via the termination involving two ^3He's as long as the cross section factor for the $^3He + ^3He$ reaction (S_{33}) is greater than 1 MeV-barn [Shaviv et al., 1967]. Any larger S_{33} will only serve to burn up the ^3He faster and does not affect the rate governing process, hence

the central temperature, etc.. The $^3He + ^3He$ rate however, strongly modifies the equilibrium concentration of the ^3He and ^7Be. Though the $^3He + ^4He$ process is relatively infrequent and does not affect the energy generation in the Sun, the subsequent reactions release high energy neutrinos. Since neutrinos interact with matter only through the weak interaction, they escape from the center of the Sun and are the only information carriers from the region of the Sun where nuclear reactions are believed to be occurring. Terrestial observation of these neutrinos would then confirm the belief in nuclear origin of stellar energy. There are three neutrino sources in the proton-proton chain. First neutrinos are liberated with positrons in the initial fusion of two protons into deuterium. These neutrinos have continuous spectra with an end point of 0.42 MeV. These are the most numerous, but such low energy neutrinos have too low a cross section for observation with the well known neutrino induced reactions. Next, there are neutrinos released in the electron capture of ^7Be and in the decay of ^8B. The ^8B neutrinos are the most energetic (end point = 14.1 MeV) and more readily observable in spite of their lower flux at the earth. The dependence of the ^8B neutrino flux as a function of the cross section factor for the $^3He + ^3He$ process will be outlined below.

Rate of nuclear processes inside stars - Inside hot matter where particle energies follow the Maxwellian distribution law, the rate of a reaction (i + j) is given by

$$R_{ij} = \langle \sigma(v)v \rangle_{ij} \frac{n_i n_j}{(1 + \delta_{ij})} \text{ reactions/unit vol./unit time.}$$

where v is the relative velocity between particles i and j (governed by the Maxwellian distribution law)

n_i and n_j are the particle densities

$\sigma(v)$ is the total reaction cross section for (i + j) with relative velocity v or relative energy = $\frac{1}{2}\mu v^2$ - (μ is the reduced mass of i + j).

The factor $(1 + \delta_{ij})$ appears because each reaction between identical particles would otherwise be counted twice.

$$\text{Defining } a_{ij} \equiv \langle \sigma(v), v \rangle_{ij} = \frac{\int_0^\infty [\sigma(v)v] e^{-\frac{\mu v^2}{2kT}} v^2 dv}{\int_0^\infty e^{-\frac{\mu v^2}{2kT}} v^2 dv}$$

for a temperature T,

$$\text{or} \quad a_{ij} = \frac{\pi}{\sqrt{\mu}} \left(\frac{2}{\pi kT}\right)^{3/2} \int_0^\infty \sigma_{ij}(E) e^{-E/kT} E dE \ .$$

For non-resonant processes

$$\sigma_{ij} \approx [S_{ij} + S'_{ij} E] \frac{1}{E} e^{-b/\sqrt{E}} \quad \text{where} \quad b = \frac{2\pi\alpha c z_i z_j \sqrt{\mu}}{\sqrt{2}}$$

$$a_{ij} \approx \frac{\pi}{\sqrt{\mu}} \left(\frac{2}{\pi kT}\right)^{3/2} \int_0^\infty [S_{ij} + S'_{ij} E] e^{-(E/kT + b/\sqrt{E})} dE \ .$$

The integral is calculated by expanding the integrand about $E = E_0$ where the integrand reaches a maximum. This value is $E_0 = (bkT/2)^{2/3}$.

$$\text{Then } a_{ij} \approx \frac{16}{9\sqrt{3}} \cdot \frac{1}{2\pi c\alpha} [S_{ij} + S'_{ij} E_0] \frac{\tau^2 e^{-\tau}}{z_i z_j \mu}$$

where

$$\tau = \frac{3E_0}{kT} .$$

The electrons inside the plasma shield the Coulomb field of the interacting nuclei to some extent. This increases the barrier penetration probability. This effect is taken into account by the quantity f_{ij}.

$$\text{Finally, } a_{ij} = 7.20 \times 10^{19} f_{ij} [S_{ij} + S'_{ij} E_0] \frac{\tau^2 e^{-\tau}}{z_i z_j A} \text{ reactions-cm}^3/\text{sec}$$

where

$$\tau = 42.48 \left(z_i^2 z_j^2 \frac{A}{T_6}\right)^{1/3} .$$

S_{ij} is expressed in keV-barns and A is the reduced mass number.

Branching ratios - The branching ratio for the termination of the p-p chain by the $^3He + {}^4He$ process is defined by

$$\beta = \frac{R_{^3He,\,^4He}}{R_{^3He,\,^3He} + R_{^3He,\,^4He}} \equiv \frac{R_{34}}{R_{33} + R_{34}} = \frac{1}{1 + (R_{33}/R_{34})}$$

$$\beta = \frac{1}{1 + a_{33} n_3 / 2 a_{34} n_4} \quad .$$

To calculate β, the concentration n_3 of ^3He is required. n_4 is the helium content.

If the concentrations are assumed to be equilibrium concentrations, the equilibrium of deuterium in the star implies $\dot{n}_2 = 0$, i.e.,

$$\frac{1}{2} a_{11} n_1^2 = a_{12} n_1 n_2$$

assuming that only one reaction is important in consuming deuterium. Equilibrium of ^3He implies $\dot{n}_3 = 0$, i.e.,

$$a_{12} n_1 n_2 = 2\left(\frac{1}{2} a_{33} n_3^2\right) + a_{34} n_3 n_4 .$$

The 2 appears in the 1st term on the right hand side since two ^3He nuclei are consumed per $^3He + {}^3He$ reaction.

Combining the two equations, one obtains

$$a_{33} n_3^2 + a_{34} n_3 n_4 - \frac{1}{2} a_{11} n_1^2 = 0 .$$

Solving for n_3; $n_3 = \frac{a_{34} n_4}{2a_{33}} \left[\sqrt{1 + \frac{2a_{11} a_{33}}{a_{34}^2} \frac{n_1^2}{n_4^2}} - 1 \right]$

$$\beta = \frac{4}{3 + \sqrt{1 + \frac{2a_{11} a_{33}}{a_{34}^2} \frac{n_1^2}{n_4^2}}} \quad .$$

If the chain terminates predominately via the $^3He + ^3He$ process

$$\frac{1}{2} a_{33} n_3^2 \gg a_{34} n_3 n_4$$

which implies

$$n_3 \approx \sqrt{\frac{a_{11}}{2a_{33}}}\, n_1 \quad \text{and} \quad \beta \approx \frac{1}{1 + \sqrt{\frac{a_{11} a_{33}}{8a_{34}^2}} \frac{n_1}{n_4}}$$

also

$$R_{34} \approx \sqrt{\frac{a_{11}}{2a_{33}}}\, a_{34} n_1 n_4 \propto \frac{1}{\sqrt{S_{33}}} \quad .$$

Thus, the rate for the $^3He + ^4He$ branch is inversely proportional to the square root of the cross section factor for the $^3He + ^3He$ process. If nearly all the energy generation occurs via the $^3He + ^3He$ termination (i.e., $\beta \ll 1$), then changes in the

value of S_{33} do not significantly affect the central temperature, etc., in the Sun. In such a case, the flux of high energy neutrinos from the decay of ^{8}B would also depend on the inverse square root of S_{33}. The present measurements yield a value of S_{33} which is about 4.5 times larger than the hitherto accepted value. The effect of this change in the value of S_{33} on the high energy neutrino flux from the Sun would be to reduce the ^{8}B neutrino flux by a factor slightly exceeding 2.

APPENDIX I

THE RECIRCULATING DIFFENTIALLY PUMPED GAS TARGET SYSTEM

The description of the system given in the main body of the text will be supplemented here with some of the more important dimensions and certain design considerations.

The target chamber is 25 cm in diameter and 15 cm deep. The canal-A is 2 cm long with a bore 3 mm in diameter. The choice of the bore diameter is such as to allow the maximum beam into the target chamber while keeping the gas flow manageable.

The gas flow in the canal has to be treated as compressible fluid flow when the ratio of the pressures at the ends of the canal exceeds a value of about 2 (in the present case this ratio is about 100). The viscous effects are negligible as long as the length of the canal is less than a few hundred diameters. The flow is potential flow and in this case the flow velocity quickly reaches Mach number one on entering the canal and stays at that velocity until leaving the canal when it gets supersonic. The gas density, pressure and temperature are all nearly constant in the canal except near the ends. The transition zone is of the order of a canal diameter. These considerations are useful not only in the design of the system but also in estimating the energy loss of the primary beam in traversing the canal.

The mass flow rate is given by

$$M = \rho A V_s$$

where M is the mass flow rate

A is the area of cross section of the canal

V_s is the velocity of sound in the medium (^{3}He)

and ρ is the density of gas where the flow velocity reaches V_s.

From thermodynamic considerations, one obtains for an adiabatic process

$$\rho = \rho_0 \left(\frac{\gamma + 1}{2}\right)^{1/1-\gamma}$$

where ρ_0 is the stagnation density (i.e., where the flow velocity is zero) or the density of gas in the target chamber and γ is the ratio of specific heats which is 1.67 for helium.

For a target pressure of 20 torr, the mass flow of ^{3}He is $\sim$ 15 mgm/sec or a volume flow of approximately 100 torr - ℓ/sec. In order to maintain a pressure of about 0.1 torr in chamber-A, pumping speeds of $\sim 10^3$ ℓ/sec are required. Besides the pumping speed requirement the pump should be operable at sufficiently high back pressures to enable recirculation of the gas. Also the exhaust should be as clean as possible. These requirements are met by a set of cascaded Roots pumps. The exhaust of these is relatively clean as the blower type pump does not use any oil except for lubrication of the bearings and gear wheels which are not seen by the gas. The pumps are a Heraeus Model R-1600 backed by a two stage Heraeus Model R-152 Roots blowers. The pumps have matched pumping speeds and the combination has about the right pumping speed. The R-152 can be operated with its output at

pressures up to a maximum of 25-30 torr. Continued operation at excessive back pressures result in overheating of the pump. This can cause seizure of the impellers.

The second canal, canal-B is 10 cm long and has a bore 3.5 mm in diameter. The gas flow through this canal is about 0.05 torr - ℓ/sec. Chamber-B is pumped by a NRC-NHS 4 oil diffusion pump. The diffusion pump is backed by the cascaded Roots pumps to minimize gas loss. The baffled NRC-NHS 4 has a pumping speed of 400 ℓ/sec at 10^{-5} torr. Typical pressures in chamber-B are a few times 10^{-5} torr.

Finally, the gas steaming out of canal-C, which is rather large ($\sim$ 10 mm in diameter and about 5 cm long), is permanently lost. The rate of gas loss is less than 1% of the total charge per hour. It is interesting to compare the gas loss with the recycling time of the gas through the system which is about 5 seconds.

The system requires a total charge of about 500 cc of ^{3}He at STP to run the target at a pressure of 20 torr. The gas can be stored in the R-152 at the end of a run with an efficiency of better than 90%.

APPENDIX II

CALORIMETRIC BEAM INTEGRATOR

Construction - The calorimetric beam integrator consists of two almost identical heat sinks in the form of copper discs, mounted co-axially in a pipe as shown in Figure 6. Brass rods which are soldered into the discs and the enclosing pipe, hold the discs in place. A heating coil and two thermistors are embedded in each of the copper discs with a hot setting epoxy. The thermistors have similar temperature - resistance characteristics. All the electrical leads are brought out through a standard 2" flange with vacuum feed throughs. The heat sinks with their enclosure are mounted on the flange with all the centers collinear. The two elements of the device are made as nearly identical as possible. Details of the components are listed at the end of this appendix.

Electrical circuit - Two thermistors, one from each heat sink form the two sides of a Wheatstone bridge. The bridge is completed by a 10 turn potentiometer and is powered by a mercury cell. The bridge balance is observed on a Hewlett-Packard milli-micro voltammeter. The electrical circuit diagram is given in Figure 7.

The Hewlett-Packard meter provides a voltage output that is directly proportional to the meter deflection. The voltage output is ± 1 volt corresponding to full scale deflections of the meter. The output of the meter is used to switch on an ultra-sensitive polarized relay. The relay [switches at a voltage of about 150 mV]

controls the power supplied to the heater coil in the dummy heat sink. The relay also starts and stops a timer simultaneously with the turning on and off of the heater in the dummy. Variable voltage D. C. power supplies are used to energize the heater coils in the heat sinks. The heater in the calorimeter is used for purposes of calibration only. The power to this is controlled by an ordinary toggle switch. The electrical power supplied to the heaters are determined by measuring the currents through and the voltages across the heating coils using a Digital voltmeter.

Operation - With both heat sinks at the same temperature, the bridge is balanced with the 10-turn potentiometer. The power supply feeding the dummy heater is turned on and the power level is set about twice as high as the estimated beam power. At this stage the dummy heater is still not energized because the power is fed to it through the relay which is open. When the beam is allowed to be incident on the calorimeter, the energy dissipated by the beam heats the calorimeter causing the thermistor resistance to change. The bridge is no longer balanced, the off balance voltage generates the output voltage in the Hewlett-Packard meter which closes the relay. The relay is a SPDT type switch with the switch closed one way for positive currents in excess of ~ 0.7 milli-amperes while the switch is closed the other way for a similar current in the opposite direction. It is essential to observe the correct polarity for the device to function. The relay should close the circuit when the calorimeter is warmer than the dummy. When the relay closes, the heating coil in the dummy is energized. Because of the larger amount of power dissipated in the dummy, the dummy warms up faster than the calorimeter causing the bridge

current to swing back. At a certain point the relay opens turning off the coil in the dummy. The cycle starts all over, with typical cycle lengths of about 4 seconds. The timer, operating with the dummy heater records the total time for which the power was on. In this manner the total energy deposited by the beam in the calorimeter is measured in terms of the total electrical energy supplied to the dummy. Ideally the two quantities should be equal but departures from complete symmetry in the construction of the two elements introduce a proportionality constant different from unity. This constant is measured by a calibration of the integration and is referred to as the calorimeter calibration constant.

Calibration - The integrator is calibrated with the beam turned off and energizing the heating element in the calorimeter with a steady D. C. source. The electrical energy spent in the calorimeter in a certain time is integrated as described above. The calibration constant is simply the ratio of the electrical energies dissipated in the calorimeter to that in the dummy.

The calibration constant is about 1. 25 for the instrument used in these measurements. The calibration constant itself is weakly dependent on the quiescent temperature of the heat sinks due to some mismatch of the thermistor characteristics. For this reason the operating temperature of the dummy is monitored by a second thermistor embedded in it. The calibration constant for each run is separately determined with a power level in the calorimeter to correspond to the same quiescent temperature.

Over the range of beam currents employed, the variation of the calibration constant was less than ± 5% about the mean.

Some component details

* Size of heat sinks - 2.2 cm (diameter) x 0.35 cm.
* Half angle subtended by calorimeter at the tip of the canal = $\pm 3.5^{o}$ (compared to R.M.S. scattering angle $< 1.5^{o}$).
* Mass of heat sinks - 7.2 gm each.
* Thermistors used - feroxcube NTC beads, type B8 320 02P/ 4K7.
* Thermistor bead size - 0.5 mm (diameter).
* Thermistor resistance - 4.7 K at 25^{o}, 1 K at 80^{o} C.
* Main relay - Barber Coleman Micropositioner (type AYLZ 7329-100).
* Maximum power level - 4 watts for the heating coils.
* Minimum operable power level - 40 milliwatts.

APPENDIX III

CALCULATION OF THE GEOMETRICAL FACTOR $\langle \Omega \ell \rangle$

The geometrical factor $\langle \Omega \ell \rangle$ will be calculated for a line beam (i.e., ignoring the finite size of the beam) and for observation at 90° to the direction of the incident beam.

The following co-ordinate system is employed (see Figure 6).

Beam along ($y = 0$, $z = D$).

Defining slits along ($x = \pm W$, $z = d$).

Counter aperture is defined by $x^2 + y^2 \leq a^2$, $z = 0$.

From Figure 6,
$$\alpha = a + \frac{D}{d}(W - a)$$
$$\beta = -a + \frac{D}{d}(W + a)$$
$$P = W - \frac{d}{D - d}(\zeta - W) \ .$$

Solid angle subtended by counter aperture at a point along the beam $(\zeta, 0, D)$ is

$$\Omega(\zeta) = \iint \frac{\vec{ds} \cdot \hat{r}}{r^2}$$
$$\vec{ds} = (dx\, dy)\,\hat{z}$$
$$= (\zeta - x)\hat{x} - y \cdot \hat{y} + D \cdot \hat{z} \ .$$

The unit vectors are denoted by a hat ($\wedge$) placed above the symbol.

Limits of integration - The circular aperture if defined by $x^2 + y^2 \leq a^2$ and for a point $0 < \zeta < \beta$ along the beam, x ranges from -a to P.

$$\Omega(\zeta) = \int_{-a}^{P} dx \int_{-\sqrt{a^2-x^2}}^{\sqrt{a^2-x^2}} dy \cdot \frac{D}{[(\zeta - x)^2 + y^2 + D^2]^{3/2}} \quad \text{for } 0 < \zeta < \beta$$

$$= 2D \int_{-a}^{P} dx \frac{\sqrt{a^2 - x^2}}{[(\zeta - x)^2 + D^2][D^2 + a^2 + \zeta^2 - 2\zeta x]} \cdot$$

This is exact. To carry out the integral, the integrand is expanded in powers of a certain small quantity.

$$\zeta < \beta \text{ and } |x| < a \qquad \left(\frac{\zeta - x}{D}\right) < \left(\frac{W + a}{D}\right) \equiv \epsilon$$

$$\text{also } \left(\frac{\zeta^2 - 2\zeta x}{D^2 + a^2}\right) < \left(\frac{W + a}{D}\right)$$

$$\Omega(\zeta) = 2D \int_{-a}^{P} dx \left[1 - \frac{3\zeta^2 - 6\zeta x + 2x^2}{2D^2} + O(\epsilon^4)\right] \frac{\sqrt{a^2 - x^2}}{D^2\sqrt{D^2 + a^2}}$$

$$\Omega(\zeta) \approx \frac{2}{D\sqrt{D^2 + a^2}} \left[\frac{1}{2}\left(1 - \frac{3\zeta^2}{2D^2} - \frac{a^2}{4D^2}\right)\left(P\sqrt{a^2 - P^2} + a^2 \sin^{-1}\frac{P}{a} + \frac{\pi a^2}{2}\right)\right.$$

$$\left. + \frac{1}{D^2}\left(\frac{P}{4} - \zeta\right)(a^2 - P^2)^{3/2}\right] \text{ for } 0 < \zeta < \beta .$$

In region 1 defined by $0 < \zeta < \alpha$, $P = +a$

$$\Omega(\zeta) \approx \frac{\pi a^2}{D^2} \left[1 - \frac{3\zeta^2}{2D^2} - \frac{3a^2}{4D^2}\right]$$

$$\int_0^{\alpha} \Omega(\zeta)d\zeta = \frac{\pi a^2}{D^2} \left[\alpha\left(1 - \frac{3a^2}{4D^2} - \frac{\alpha^2}{2D^2}\right)\right] .$$

In region 2 defined by $\alpha < \zeta < \beta$

$$P = W - \frac{d}{D - d}(\zeta - W)$$

$$\text{or } \zeta = \lambda P + \mu \quad \text{where } \lambda = \frac{d - D}{d} \quad \text{and } \mu = \frac{WD}{d} .$$

Since there is a one-to-one correspondence between ζ and P,

$$\int_{\alpha}^{\beta} \Omega(\zeta)d\zeta = \lambda \int_{a}^{-a} \Omega(p)dp = -2\lambda \int_{0}^{a} \text{even}[\Omega(p)]dp$$

$$\int_{\alpha}^{\beta} \Omega(\zeta)d\zeta \approx \frac{-4\lambda}{D^2} \int_0^a \left[\frac{1}{2}\left(1 - \frac{3\mu^2}{2D^2} - \frac{3a^2}{4D^2}\right)\frac{\pi a^2}{2} - \frac{3\lambda^2}{4D^2} \cdot \frac{\pi a^2}{2} P^2 \right.$$

$$\left. - \frac{3\lambda\mu}{2D^2} a^2 P \sin^{-1}\frac{P}{a} - \frac{3\lambda\mu}{2D^2} P^2\sqrt{a^2 - P^2} - \frac{\mu}{D^2}(a^2 - P^2)^{3/2}\right] dp$$

$$\approx \frac{\pi a^2}{D^2}(-\lambda a)\left[1 - \frac{3a^2}{4D^2} - \frac{(\lambda a + \mu)^2}{2D^2} - \frac{\mu^2}{D^2} - \frac{\lambda\mu a}{8D^2} - \frac{3\mu a}{4D^2}\right] .$$

Finally, $\int_0^{\beta} \Omega(\zeta)d\zeta = \left[\int_0^{\alpha} + \int_{\alpha}^{\beta}\right] (\Omega(\zeta)d\zeta)$ and $\alpha = \lambda a + \mu$

$$= \frac{\pi a^2}{D^2}\,\mu\left[1 - \frac{3(\lambda - 1)}{4D^2}\,a^2 - \frac{3\lambda^2 a^2}{8D^2} - \frac{\mu^2}{2D^2}\right]$$

$$= \frac{\pi a^2}{D}\,\frac{W}{d}\left[1 - \frac{W^2}{2d^2} - \frac{3a^2}{8D^2} - \frac{3a^2}{8d^2}\right] + O(\epsilon^4)$$

$$\langle \Omega \ell \rangle_{90^o} = \int_{-\beta}^{\beta} \Omega(\zeta)d\zeta = \frac{\pi a^2(2W)}{D \cdot d}\left[1 - \frac{W^2}{2d^2} - \frac{3a^2}{8D^2} - \frac{3a^2}{8d^2}\right] + O(\epsilon^4).$$

The angular spread - The total angular spread is calculated by determining the separate angular spreads due to the finite size of the detector and due to the finite size of the beam path observed.

The mean square angular spread due to finite detector size is given by

$$\Delta\psi_1^2 = \frac{\int_0^a \varphi^2(\rho) \cdot 2\pi\rho d\rho}{\int_0^a 2\pi\rho d\rho}$$

where $\varphi(\rho)$ is the angle measured with respect to the mean direction of observation. ρ is the radial distance from the center of detector.

$$\varphi(\rho) \approx \frac{\rho}{D} \qquad \Delta\psi_1^2 = \frac{a^2}{2D^2} .$$

The mean square angular spread due to finite length of the beam observed is given by:

$$\Delta\psi_2^2 = \frac{\int_{-\beta}^{\beta} \varphi^2(\zeta)\,\Omega(\zeta)\,d\zeta}{\int_{-\beta}^{\beta} \Omega(\zeta)\,d\zeta}$$

$$\varphi(\zeta) \approx \frac{\zeta}{D} \qquad \Delta\psi_2^2 = \frac{1}{3D^2}\left[\frac{D^2}{d^2} W^2 + a^2\left(\frac{D}{d} - 1\right)^2\right] .$$

The total mean square spread is

$$\Delta\psi^2 = \Delta\psi_1^2 + \Delta\psi_2^2 = \frac{1}{D^2}\left[\frac{a^2}{2} + \frac{a^2}{3}\left(\frac{D}{d} - 1\right)^2 + \frac{D^2}{3d^2} W^2\right].$$

Finally, the root mean square angular spread is

$$\Delta\psi = \frac{1}{D}\left[\frac{a^2}{2} + \frac{a^2}{3}\left(\frac{D}{d} - 1\right)^2 + \frac{D^2}{3d^2} W^2\right]^{1/2} .$$

REFERENCES

Agnew, H. M., Leland, W. T., Argo, H. V., Crews, R. W., Hemmendinger, A. H., Scott, W. E., Taschek, R. F., Phys. Rev. 84, 862 (1951).

Bacher, A. D., Ph.D. Thesis, California Institute of Technology, (1967).

Bacher, A. D. and Tombrello, T. A., Rev. Mod. Phys. 37, 433 (1965).

Bacher, A. D. and Tombrello, T. A., Private Communication (1967) - to be published.

Bahcall, J. N., Bahcall, N. A. and Shaviv, G., Phys. Rev. Letters - to be published.

Bethe, H. A., Phys. Rev. 55, 434 (1939).

Bethe, H. A. and Critchfield, C. L., Phys. Rev. 54, 248 (1938).

Cohen-Ganouna, J., Lambert, M. and Schmouker, J., Nucl. Phys. 40, 82 (1963).

Davis, R., Jr., Phys. Rev. Letters 12, 303 (1964).

Fowler, W. A., Phys. Rev. 81, 655 (1951).

Fowler, W. A., Ap. J. 127, 551 (1958).

Good, W. M., Kunz, W. E. and Moak, C. D., Phys. Rev. 83, 845 (1951).

Good, W. M., Kunz, W. E. and Moak, C. D., Phys. Rev. 94, 87 (1953).

Govorov, A. M., Ka-Yeng, Li , Osetinskii, G. M., Salatskii, V. I. and Sizov, I. V., JETP 15, 266 (1962).

Jarmie, N. and Allen, R. C., Phys. Rev. 111, 1121 (1958).

May, R. M. and Clayton, D. D., Ap. J. (1968) - to be published.

Neng-Ming, Wang, Novatskii, V. N., Osetinskii, G. M., Nai-Kung, Chien and Chepurchenko, I. A., J. Nucl. Phys. (USSR) 3, 1064 (1966).

Parker, P. D., Bahcall, J. N. and Fowler, W. A., Ap. J. 139, 602 (1964).

Salpeter, E. E., Phys. Rev. 88, 547 (1952).

Schatzman, E., Compt. rend. 232, 1740 (1951).

Shaviv, G., Bahcall, J. N. and Fowler, W. A., Ap. J. 150, 725 (1967).

Whaling, W., Handbuch der Physik 34, 193 (1958).

Yarnell, J. L., Lovberg, R. H. and Stratton, W. R., Phys. Rev. 90, 292 (1953).

Youn, Li Ga, Osetinskii, G. M., Sodnom, N., Govorov, A. M., Sizov, I. V. and Salatskii, V. I., JETP 12, 163 (1961).

TABLE 1

Geometrical Parameters

The values of the parameters describing the counter geometry [see pages 17-19] are given for the different slit systems used. The symbols have the following meaning:

$2W$ - Width of the front slit.

$2a$ - Diameter of the rear aperture.

D - Distance between rear aperture and center of target.

d - Distance between rear aperture and front slit.

2β - Total length of the target observed by the counter telescope at 90^{o} to the beam direction.

$\langle \Omega \ell \rangle_{90^{o}} \approx \frac{\pi a^{2}(2W)}{D \cdot d}$ - The geometrical factor.

$\Delta\psi$ - The root mean square angular spread of the counter telescope at 90^{o} to the beam direction.

TABLE 1

Geometrical Parameters

Parameter	System # 1	System # 2	System # 3	System # 4
2W	4.32 mm	4.30 mm	1.50 mm	2.55 mm
2a	11.05 mm	11.05 mm	11.05 mm	11.05 mm
D	80.5 mm	80.5 mm	80.5 mm	80.5 mm
d	67.5 mm	69.0 mm	67.8 mm	67.5 mm
2β	7.3 mm	6.9 mm	3.9 mm	5.2 mm
$\langle \Omega \ell \rangle_{90^o}$	7.62×10^{-3} st-cm	7.42×10^{-3} st-cm	2.64 st-cm	4.50 st-cm
$\Delta\psi$	3.0^o	3.0^o	2.8^o	2.9^o

Effect of second order terms in $\langle \Omega \ell \rangle_{90^o} \simeq 0.5\%$.

Precision of absolute angle determination $\sim \pm 2^o$.

TABLE 2

$^{40}A(p, p)^{40}A$ Differential Cross Sections

The measured differential cross sections for the elastic scattering of protons from argon-40 are compared with the Rutherford cross sections for the proton energies and scattering angles indicated. These measurements were made to ascertain the accuracy of the beam integration device. For additional details see pages 14-15.

TABLE 2

$^{40}A(p, p)^{40}A$ Differential Cross Sections

Proton Energy (MeV)	Laboratory Angle (Deg)	Diff. C.S. (Experimental) (mb/sr)	Rutherford C.S. (Calc.) (mb/sr)
2.00	140	155	140
1.50	140	251	249
1.00	140	563	559
0.584	130	1770	1880
0.505	130	2430	2520
0.409	130	3580	3840
0.510	90	6200	6460
0.505	90	6450	6590

TABLE 3

$^{3}He(^{3}He, 2p)^{4}He$ Total Cross Sections

The measured values of the total cross section together with the estimated total errors (statistical and systematic) are tabulated in the following table. For details see pages 29-30 and 33-36.

TABLE 3

$^{3}He(^{3}He, 2p)^{4}He$ Total Cross Sections

E_{cm} (MeV)	$\sigma(E_{cm})$ (mb.)	Error in $\sigma(E_{cm})$ (mb.)	
0.0798	0.0024	+0.0004	-0.0004
0.090	0.0051	+0.0008	-0.0006
0.096	0.0069	+0.001	-0.0008
0.096	0.0070	+0.001	-0.0008
0.125	0.043	+0.006	-0.004
0.130	0.050	+0.007	-0.005
0.145	0.100	+0.014	-0.009
0.150	0.119	+0.016	-0.012
0.156	0.136	+0.019	-0.014
0.171	0.229	+0.030	-0.023
0.192	0.33	+0.04	-0.03
0.192	0.33	+0.04	-0.03
0.195	0.41	+0.05	-0.04
0.194	0.40	+0.05	-0.04
0.195	0.39	+0.05	-0.04
0.195	0.37	+0.05	-0.04
0.221	0.67	+0.09	-0.07
0.221	0.76	+0.10	-0.07
0.237	0.79	+0.10	-0.08
0.239	0.87	+0.11	-0.09
0.244	1.03	+0.13	-0.10
0.244	1.12	+0.14	-0.11

$^{3}He(^{3}He, 2p)^{4}He$ Total Cross Sections (Cont.)

E_{cm} (MeV)	$\sigma(E_{cm})$ (mb.)	Error in $\sigma(E_{cm})$ (mb.)	
0.245	1.05	+0.14	-0.11
0.271	1.44	+0.19	-0.13
0.288	1.76	+0.23	-0.16
0.295	2.0	+0.3	-0.2
0.321	2.6	+0.3	-0.25
0.339	3.3	+0.4	-0.3
0.344	3.1	+0.4	-0.3
0.344	3.0	+0.4	-0.3
0.346	3.2	+0.4	-0.3
0.366	4.0	+0.5	-0.4
0.371	4.5	+0.6	-0.45
0.372	4.0	+0.5	-0.4
0.372	4.0	+0.5	-0.4
0.389	4.8	+0.6	-0.5
0.397	5.0	+0.6	-0.5
0.422	5.7	+0.7	-0.6
0.441	6.3	+0.8	-0.6
0.447	6.5	+0.8	-0.6
0.473	7.6	+1.0	-0.7
0.490	8.1	+1.0	-0.8
0.491	8.5	+1.1	-0.8
0.491	8.3	+1.1	-0.8
0.492	8.6	+1.2	-0.8
0.494	9.4	+1.3	-0.9

$^{3}He(^{3}He, 2p)^{4}He$ Total Cross Sections (Cont.)

E_{cm} (MeV)	$\sigma(E_{cm})$ (mb.)	Error in $\sigma(E_{cm})$ (mb.)	
0.495	7.2	+1.2	-0.8
0.495	8.3	+1.1	-0.8
0.496	8.0	+1.1	-0.8
0.498	8.0	+1.1	-0.8
0.592	11.9	+1.5	-1.0
0.693	15.8	+2.0	-1.4
0.745	19.3	+2.5	-1.8
0.747	14.8	+2.5	-1.8
0.747	19.4	+2.5	-1.8
0.794	18.9	+2.5	-1.8
0.895	23.0	+3.0	-2.1
0.993	29.9	+4.0	-2.6
0.996	27.0	+3.5	-2.5
0.996	27.0	+3.5	-2.5
0.996	29.3	+3.5	-2.5
0.999	25.9	+3.5	-2.5
0.999	30.6	+3.5	-2.5
1.001	28.4	+3.5	-2.5
1.002	28.8	+3.5	-2.5
1.051	27.5	+3.5	-2.5
1.097	30.9	+3.7	-2.6
1.102	31.9	+3.7	-2.6

TABLE 4

$^{3}He(^{3}He, 2p)^{4}He$ Cross Section Factors

The experimentally determined cross section factors along with the estimated total errors (systematic and statistical) are tabulated in the following table. For details see pages 30-31 and 33-38.

TABLE 4

$^{3}He(^{3}He, 2p)^{4}He$ Cross Section Factors

E_{cm} (MeV)	$S(E_{cm})$ (MeV-barns)	Error in $S(E_{cm})$ (MeV-barns)	
0.0798	5.57	+1.15	-0.95
0.090	4.97	+0.85	-0.68
0.096	4.45	+0.72	-0.61
0.096	4.51	+0.73	-0.61
0.125	5.13	+0.76	-0.54
0.130	4.64	+0.68	-0.51
0.145	5.15	+0.75	-0.51
0.150	5.02	+0.69	-0.54
0.156	4.68	+0.67	-0.51
0.171	4.97	+0.67	-0.52
0.192	4.22	+0.56	-0.44
0.192	4.17	+0.54	-0.42
0.195	4.91	+0.63	-0.49
0.194	4.77	+0.64	-0.50
0.195	4.61	+0.62	-0.48
0.195	4.36	+0.60	-0.44
0.221	4.61	+0.61	-0.48
0.221	5.2	+0.7	-0.5
0.237	4.1	+0.5	-0.4
0.239	4.4	+0.6	-0.4
0.244	4.7	+0.6	-0.5
0.244	5.1	+0.6	-0.5

$^{3}He(^{3}He, 2p)^{4}He$ Cross Section Factors (Cont.)

E_{cm} (MeV)	$S(E_{cm})$ (MeV-barns)	Error in $S(E_{cm})$ (MeV-barns)	
0.245	4.7	+0.6	-0.5
0.271	4.5	+0.6	-0.4
0.288	4.4	+0.6	-0.4
0.295	4.5	+0.6	-0.5
0.321	4.4	+0.6	-0.4
0.339	4.7	+0.6	-0.5
0.344	4.3	+0.6	-0.4
0.344	4.1	+0.6	-0.4
0.346	4.3	+0.5	-0.4
0.366	4.5	+0.6	-0.5
0.371	4.9	+0.6	-0.5
0.372	4.3	+0.6	-0.4
0.372	4.3	+0.6	-0.4
0.389	4.5	+0.6	-0.5
0.397	4.4	+0.6	-0.4
0.422	4.3	+0.6	-0.4
0.441	4.2	+0.6	-0.4
0.447	4.2	+0.5	-0.4
0.473	4.2	+0.6	-0.4
0.490	4.1	+0.5	-0.4
0.491	4.3	+0.6	-0.4
0.491	4.2	+0.6	-0.4
0.492	4.3	+0.6	-0.4
0.494	4.7	+0.7	-0.5

$^{3}He(^{3}He, 2p)^{4}He$ Cross Section Factors (Cont.)

E_{cm} (MeV)	$S(E_{cm})$ (MeV-barns)	Error in $S(E_{cm})$ (MeV-barns)	
0.495	3.6	+0.6	-0.4
0.495	4.1	+0.5	-0.4
0.496	4.0	+0.5	-0.4
0.498	3.9	+0.5	-0.4
0.592	3.9	+0.5	-0.3
0.693	3.8	+0.5	-0.3
0.745	4.0	+0.5	-0.4
0.747	3.1	+0.5	-0.4
0.747	4.0	+0.5	-0.4
0.794	3.5	+0.5	-0.3
0.895	3.5	+0.5	-0.3
0.993	3.9	+0.5	-0.3
0.996	3.5	+0.5	-0.3
0.996	3.5	+0.5	-0.3
0.996	3.8	+0.5	-0.3
0.999	3.4	+0.5	-0.3
0.999	4.0	+0.5	-0.3
1.001	3.7	+0.5	-0.3
1.002	3.7	+0.5	-0.3
1.051	3.3	+0.4	-0.3
1.097	3.5	+0.4	-0.3
1.102	3.6	+0.4	-0.3

TABLE 5

Summary of Errors

The following table summarizes the statistical and systematic errors considered in Chapter IV. For details see pages 33-38.

TABLE 5

Summary of Errors - Systematic and Relative

Quantity	Source	Relative Error	Systematic Error
N_B	Total energy spent in calorimeter	± 4%	± 3%
	Beam energy at calorimeter	± 3%	± 4%
n_T	Impurities	-	-1%, +0%
	Pressure measurement	± 2%	± 2%
	Pressure variation near target region	-	-3%(?), +0%
	Temperature	-	-1%, +0%
Y	Counting statistics, dead time, background	± 3%	-
	Low energy protons (not obs.)	-	± 2%
$\langle \Omega \ell \rangle$	Alignment, dimensions and distances	± 2%	± 3%
	Angle setting	-	±6% at 30° 0% at 90°
	Angular distribution effects	-	± 2%
$\sigma(E)$	All effects listed above (gross)	± 7%	+ 10% - 7%
E	Energy calibration	-	± 1 keV
	Energy loss	± 1 keV	± 2 keV
	Energy spread	-	-
E	Total	± 1 keV	± 2.5 keV

TABLE 6

Errors in S_0 and S_1

The errors in S_0 and S_1 are listed in the following table for fits of the experimentally determined cross section factors to a linear function of energy over three different energy ranges. For details see page 38.

TABLE 6

Errors in S_0 and S_1

Energy Range	S_0, S_1	Statistical Error	Systematic Error	Total Error
E_{cm} < 200 keV	S_0 = 5.3 MeV-b	± 0.6	+0.58, -0.37	+0.9, -0.7
	S_1 = - 3.7 b	± 3.4	-	± 3.4
E_{cm} < 350 keV	S_0 = 5.0 MeV-b	± 0.3	+0.55, -0.35	+0.65, -0.45
	S_1 = -2.1 b	± 1.1	-	± 1.1
E_{cm} < 500 keV	S_0 = 5.0 MeV-b	± 0.2	+0.55, -0.35	+0.6, -0.4
	S_1 = -1.8 b	± 0.5	-	± 0.5

FIGURE 1

The Differentially Pumped Gas Target System

The figure shows a horizontal section of the differentially pumped gas target system with the counter telescope positioned at 45^{o} to the direction of the beam. In this section the support for the counter telescope and the anode wire of the proportional counter are not visible. A detailed description of the system may be found on pages 9-12 and 53-55.

FIGURE 1

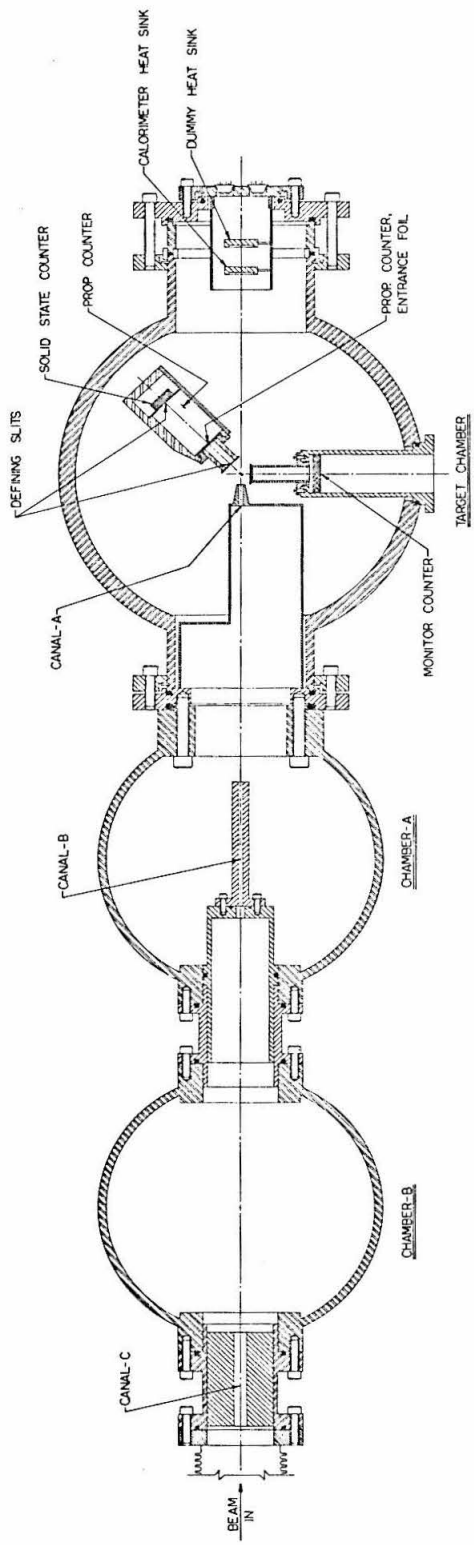
CALORIMETER HEAT SINK
DUMMY HEAT SINK
PROP COUNTER
SOLID STATE COUNTER
PROP COUNTER, ENTRANCE FOIL
DEFINING SLITS
TARGET CHAMBER
MONITOR COUNTER
CANAL-A
CANAL-B
CHAMBER-A
CHAMBER-B
CANAL-C
BEAM IN

FIGURE 2

The Differentially Pumped Gas Target System

The figure shows a vertical section of the DPGT system with the counter telescope situated at 90^{o} to the incident beam direction. Also shown is a schematic of the recovery and recirculation system. For details see pages 9-12 and 53-55.

FIGURE 2

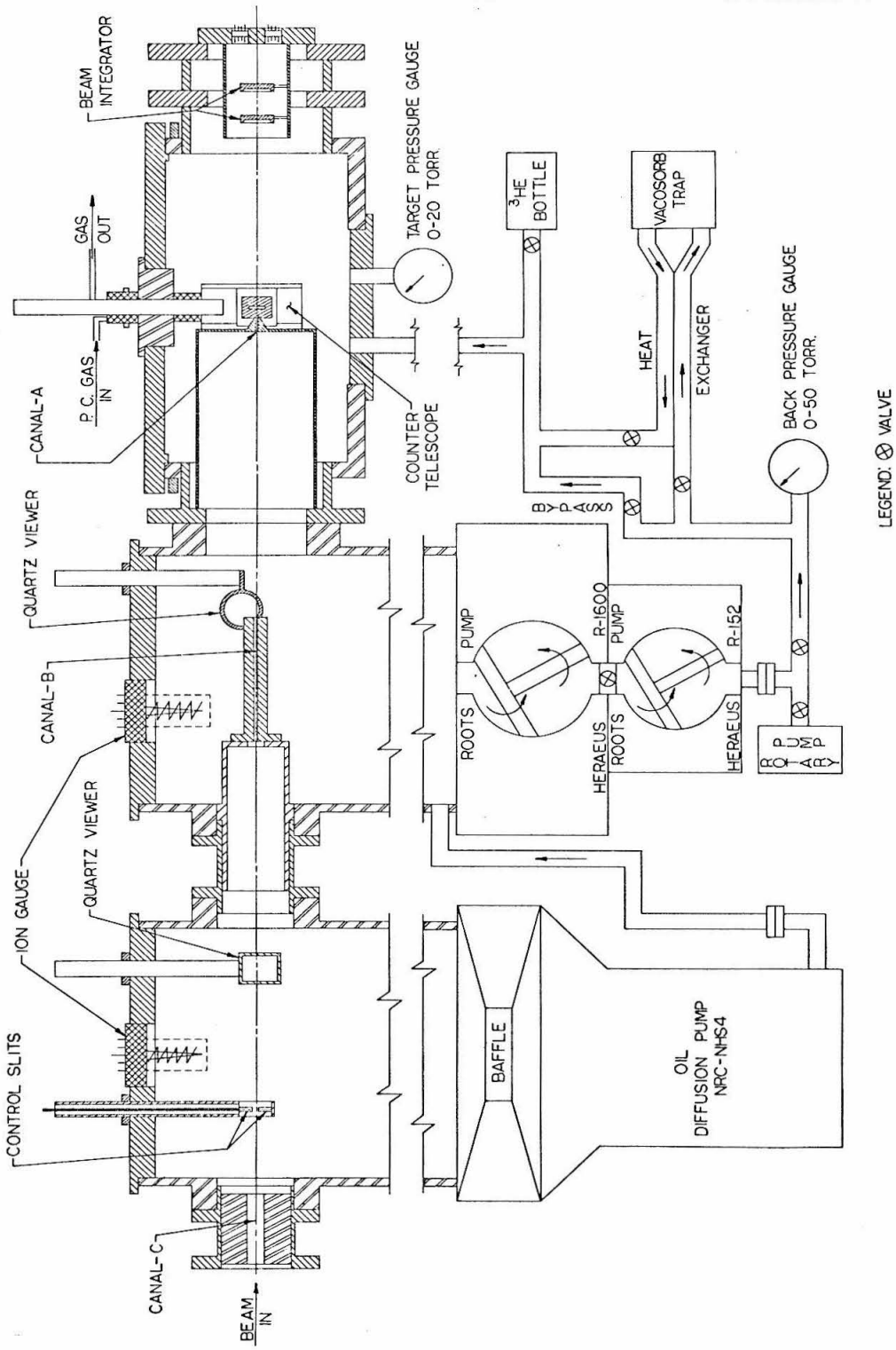
BEAM INTEGRATOR
GAS OUT
P.C. GAS IN
CANAL-A
QUARTZ VIEWER
CANAL-B
QUARTZ VIEWER
ION GAUGE
CONTROL SLITS
CANAL-C
BEAM IN
TARGET PRESSURE GAUGE 0-20 TORR
COUNTER TELESCOPE
^{3}HE BOTTLE
VACOSORB TRAP
HEAT EXCHANGER
BACK PRESSURE GAUGE 0-50 TORR.
BYPASS
PUMP
ROOTS
HERAEUS
R-1600 PUMP
R-152
HERAEUS
ROOTS
ROUGHING PUMP
BAFFLE
OIL DIFFUSION PUMP NRC-NHS4
LEGEND: ⊗ VALVE

FIGURE 3

The Counter Telescope

The counter telescope consisting of the gas proportional counter and the surface barrier detector is shown. The beam direction, indicated by a circular spot, is perpendicular to the plane of the figure. The front slit that defines the target thickness is shown separately in End View. The counter telescope is described in detail on pages 15-17.

FIGURE 3

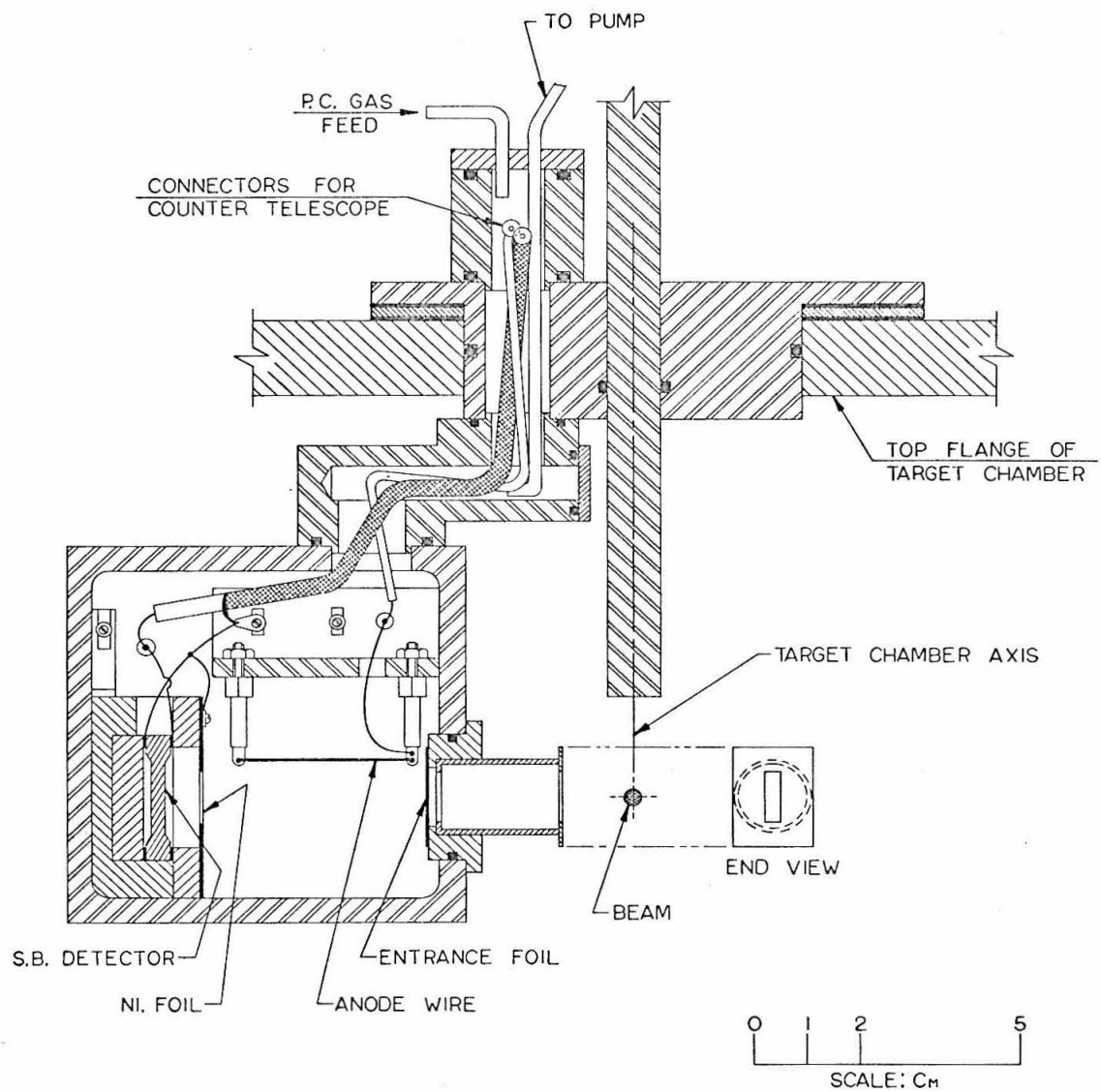
TO PUMP
P.C. GAS FEED
CONNECTORS FOR COUNTER TELESCOPE
TOP FLANGE OF TARGET CHAMBER
TARGET CHAMBER AXIS
END VIEW
BEAM
S.B. DETECTOR
NI. FOIL
ANODE WIRE
ENTRANCE FOIL
0 1 2 5
SCALE: Cm

FIGURE 4

Counter Geometry

The figure shows the target region as defined by the circular aperture in front of the solid state counter and the rectangular slit, for a detection angle ψ. See pages 17-19.

FIGURE 4

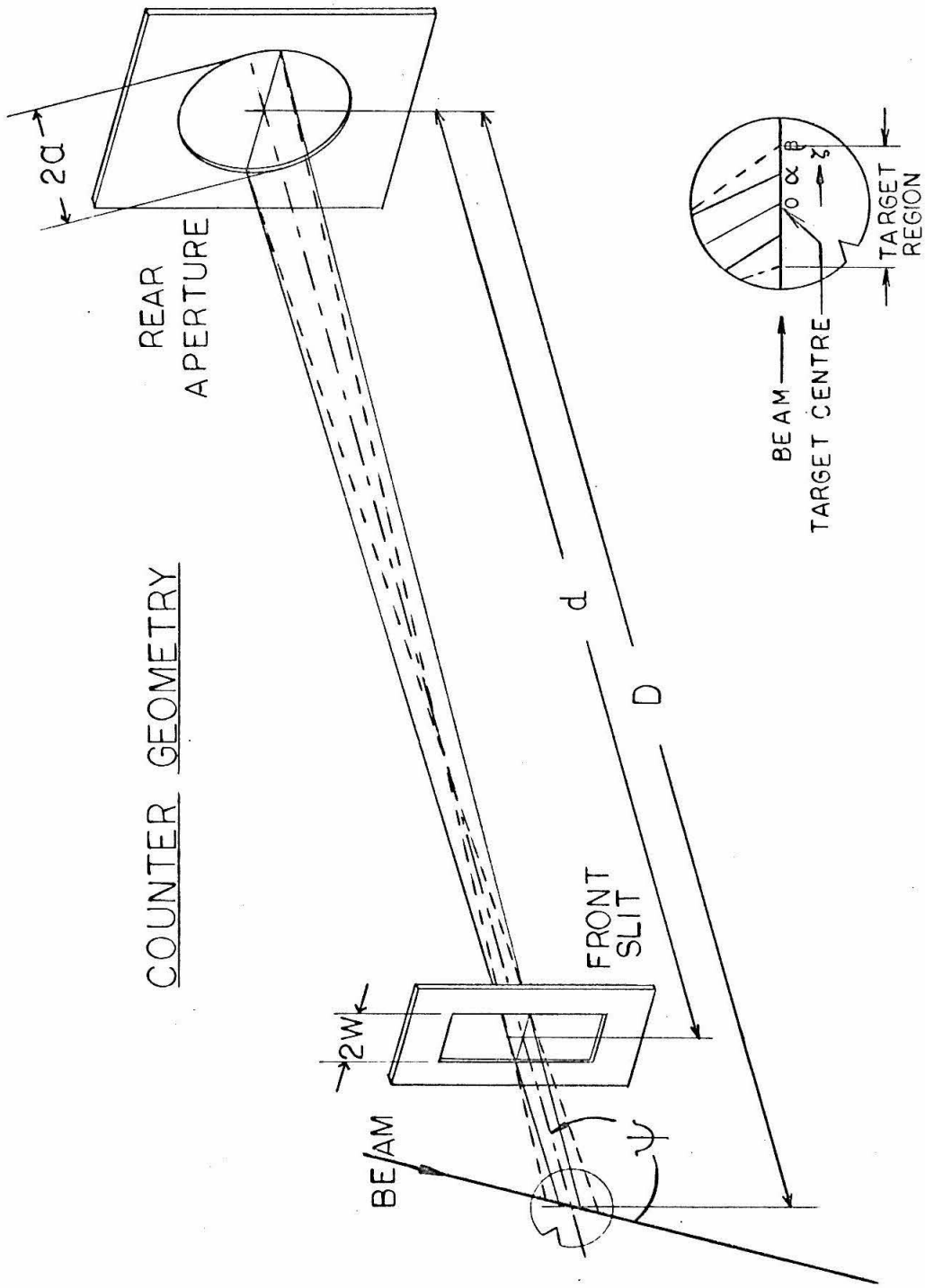
COUNTER GEOMETRY
2a
REAR APERTURE
d
D
FRONT SLIT
2W
BEAM
ψ
BEAM
TARGET CENTRE
α β
ζ
TARGET REGION

FIGURE 5

Counter Geometry

(a) and (b) The figure shows co-ordinate system employed for calculating the geometrical factor. See pages 60-64.

(c) The figure shows the variation of the solid angle, $\Omega(\zeta)$, subtended by the detector as a function of the distance ζ, along the beam, measured from the center of the target chamber. See pages 17-19.

FIGURE 5

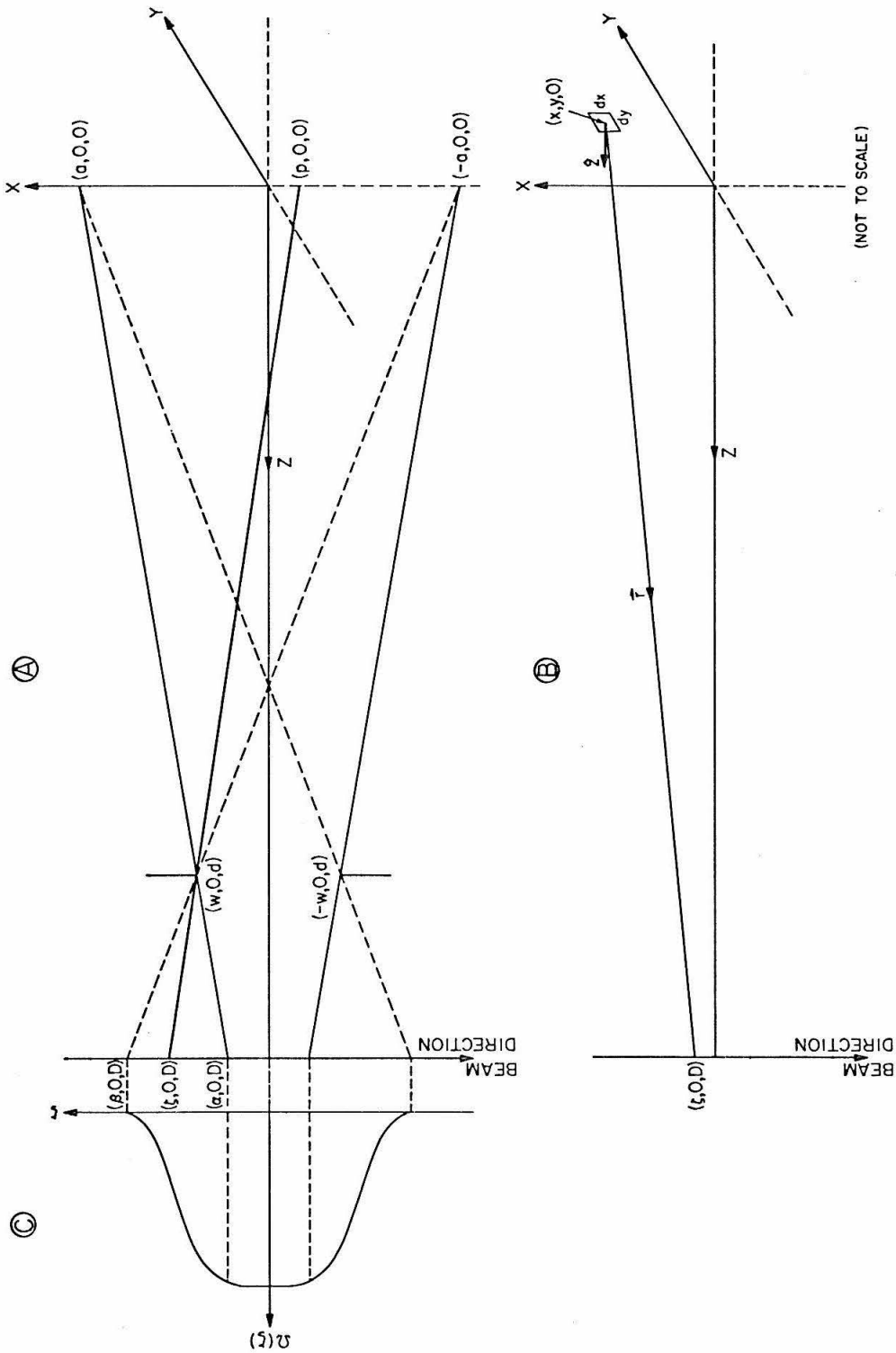
Y
X
Z
(a,0,0)
(p,0,0)
(-a,0,0)
(w,0,d)
(-w,0,d)
BEAM DIRECTION
(β,0,D)
(ζ,0,D)
(α,0,D)
ξ
Ω(ζ)
A
B
C
(x,y,0)
dx
dy
ξ
r
(NOT TO SCALE)

FIGURE 6

The Calorimetric Beam Integrator

The figure shows a sectional view of the beam integrating device. Positioning of the thermistors and the heating coil in each of the heat sinks is shown separately. For a detailed description of the calorimetric beam integrator see pages 56-59.

FIGURE 6

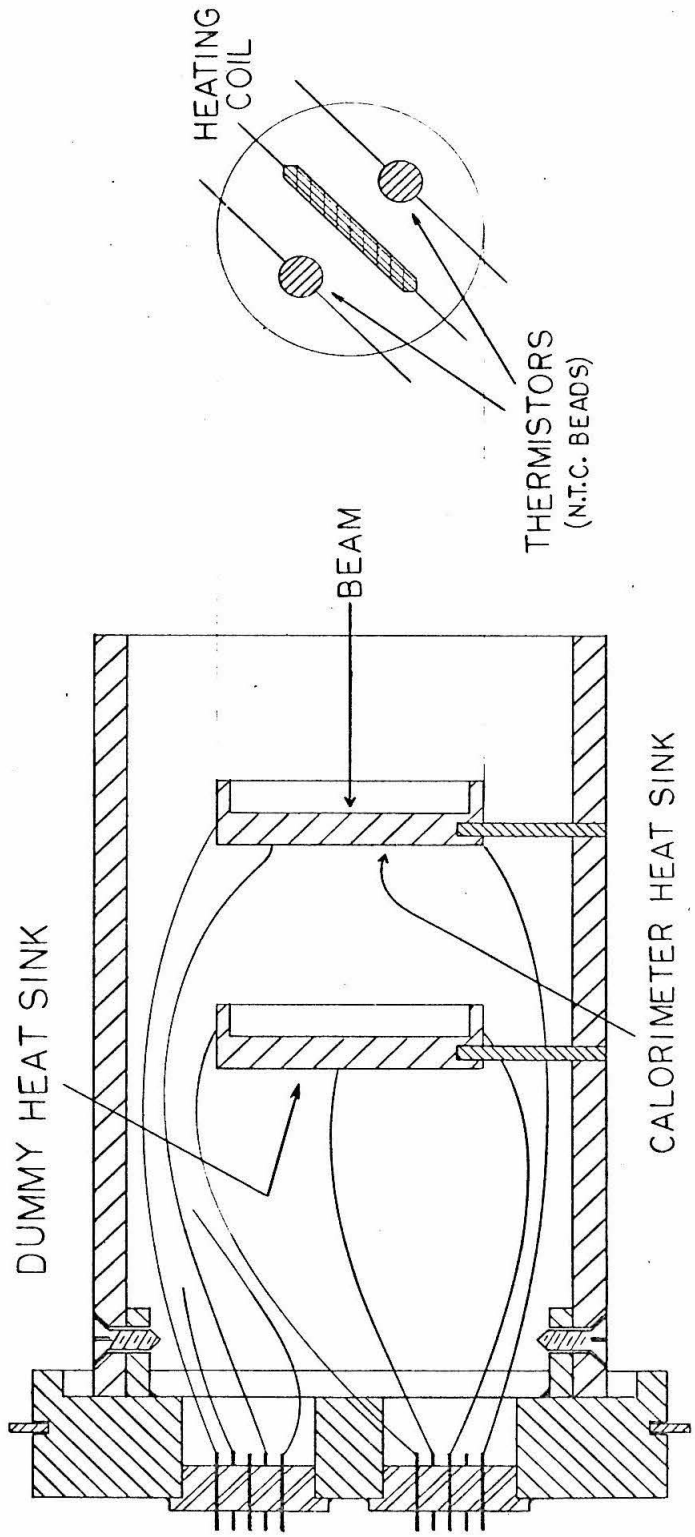
HEATING COIL
THERMISTORS (N.T.C. BEADS)
BEAM
DUMMY HEAT SINK
CALORIMETER HEAT SINK

FIGURE 7

Circuit Diagram for Beam Integrator

The figure shows the electrical circuit for the beam integrator. The abbreviation D. V. is used for digital voltmeter. For details, see pages 56-59.

FIGURE 7

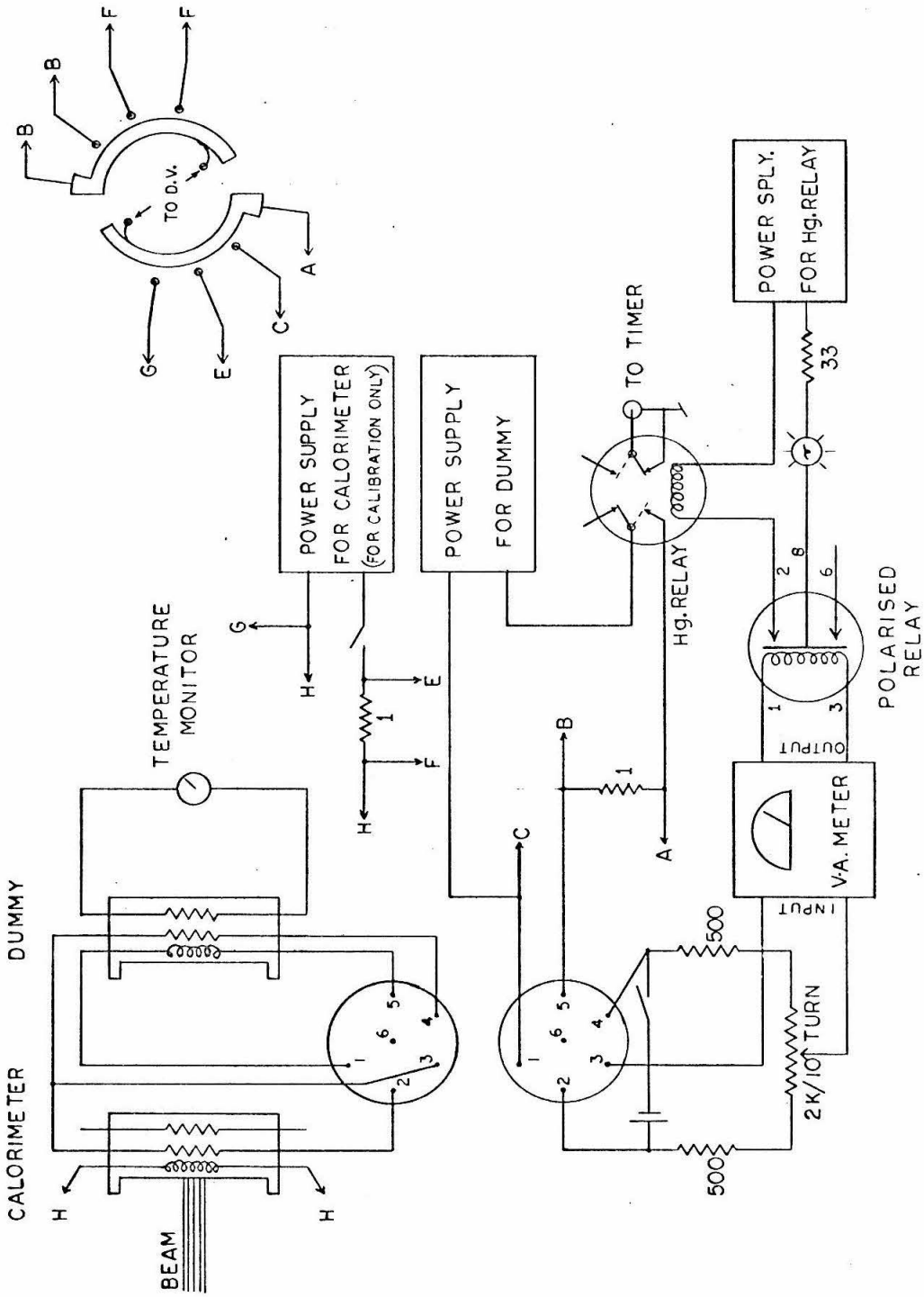
B
B
F
F
TO D.V.
A
C
G
E
POWER SUPPLY
FOR CALORIMETER
(FOR CALIBRATION ONLY)
POWER SUPPLY
FOR DUMMY
TO TIMER
POWER SPLY.
FOR Hg. RELAY
33
Hg. RELAY
TEMPERATURE
MONITOR
G
H
E
F
1
2
8
6
1
3
OUTPUT
POLARISED
RELAY
V.A. METER
INPUT
DUMMY
CALORIMETER
BEAM
H
H
500
2K/10 TURN
500

FIGURE 8

Block Diagram of Electronics

A block diagram of the electronics used for measuring the particle spectra is shown in the figure. The following abbreviations are used:

SSC - Solid State Counter, Prop. Counter - Proportional Counter

P - Preamplifier A - Linear Amplifier

S. C. A. - Single Channel Analyzer M. C. A. - Multi-channel Analyzer

P. S - Pulse Shaper

FIGURE 8

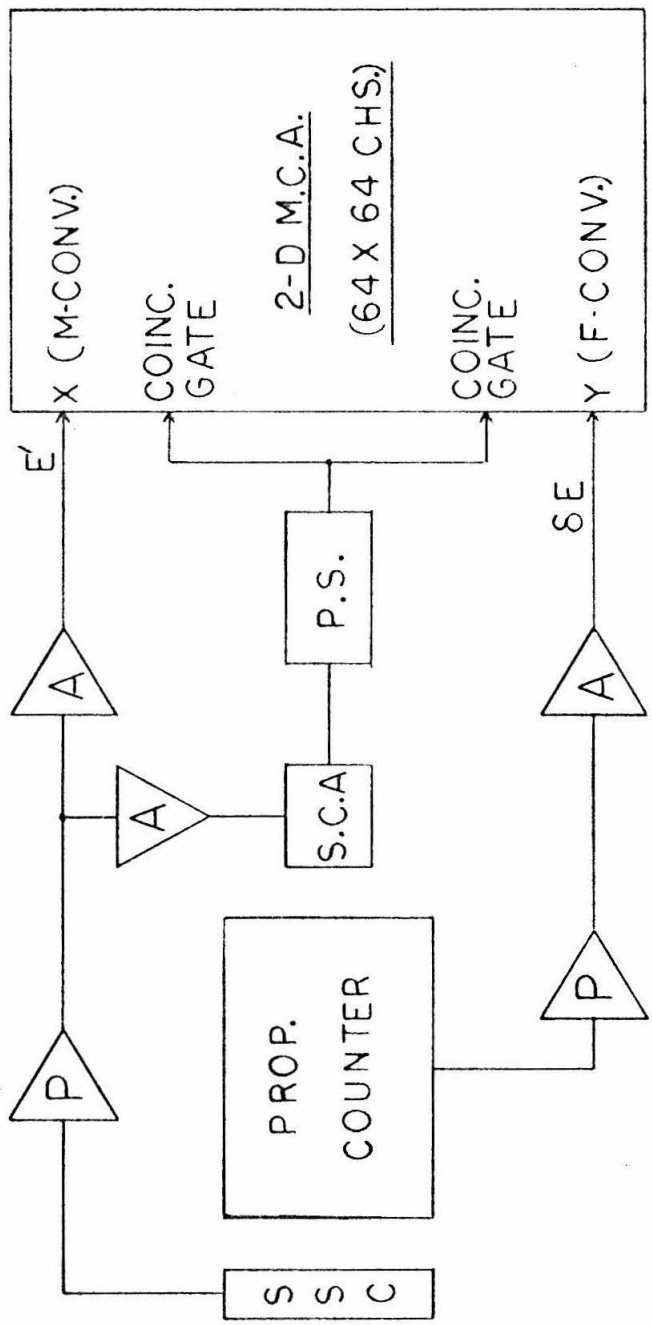
2-D M.C.A.
(64 X 64 CHS.)
X (M-CONV.)
COINC. GATE
COINC. GATE
Y (F-CONV.)
E'
δE
P.S.
A
A
A
S.C.A
P
P
PROP. COUNTER
S
S
C

FIGURE 9

CRT Display

The figure shows a two-dimensional pulse-height spectrum. The proportional counter signal is carried along the ordinate and the signal from the solid state counter along the abscissa. The two tracks in the δE - E' plane where counts are accumulated correspond to the protons and alpha particles. For details see page 21.

FIGURE 9

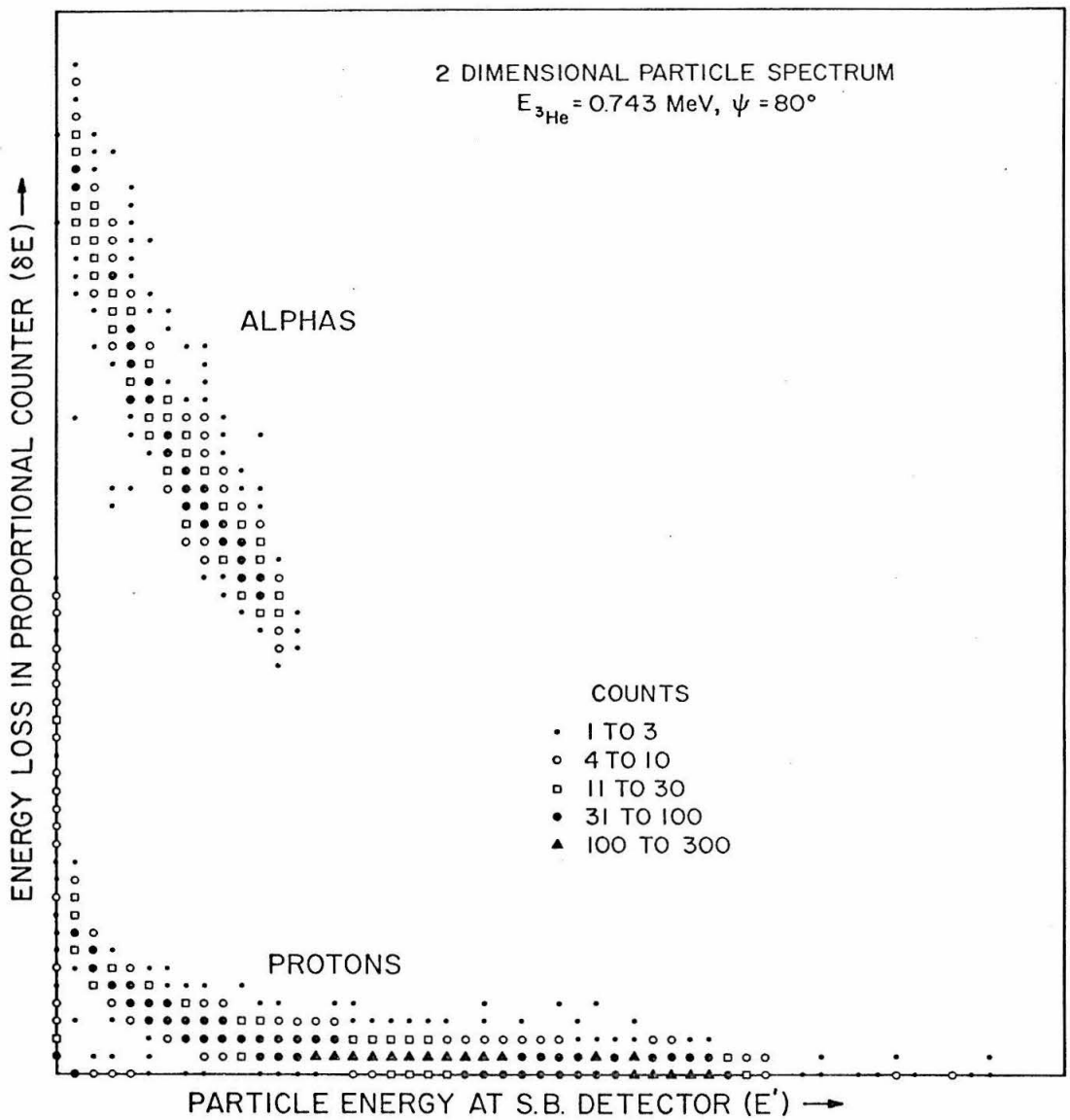
2 DIMENSIONAL PARTICLE SPECTRUM
$E_{^3He}$ = 0.743 MeV, ψ = 80°
ALPHAS
PROTONS
COUNTS
1 TO 3
4 TO 10
11 TO 30
31 TO 100
100 TO 300
ENERGY LOSS IN PROPORTIONAL COUNTER (δE) ⟶
PARTICLE ENERGY AT S.B. DETECTOR (E') ⟶

FIGURES 10-15

Proton Spectra

Figures 10-15 show proton spectra at several bombarding energies ($E_{^3He}$) and laboratory angles (ψ). The energies and angles at which individual spectra have been obtained are shown in the figures.

The arrow at a proton energy ~ 600 keV indicates the lower limit of proton energies observed by the counter telescope. Counting statistics are shown for a few representative points. Protons from the $d(^3He, p)^4He$ reaction appear as a strong sharp group beyond the three body end point in a few measurements made after previous measurements with a deuterium target. These are shown in Figures 12 and 13. At $E_{^3He} = 0.49$ MeV [Figure 13] where the protons from $d(^3He, p)^4He$ reaction is most prominent, the differential cross section for this reaction is ~ 600 times larger than the differential cross section for $^3He(^3He, 2p)^4He$. A deuterium contamination of less than 100 ppm is sufficient to produce such a strong proton group. For most other measurements the proton group from the deuterium contamination is barely noticeable. The dashed curves of Figures 13, 14 and 15 are spectra calculated by assuming a statistical distribution and isotropic angular distribution in the center-of-mass system. For further details see pages 20-22.

FIGURE 10

Proton Spectra at 1.99 and 1.49 MeV, 90^{o}

(For details see page 101.)

FIGURE 10

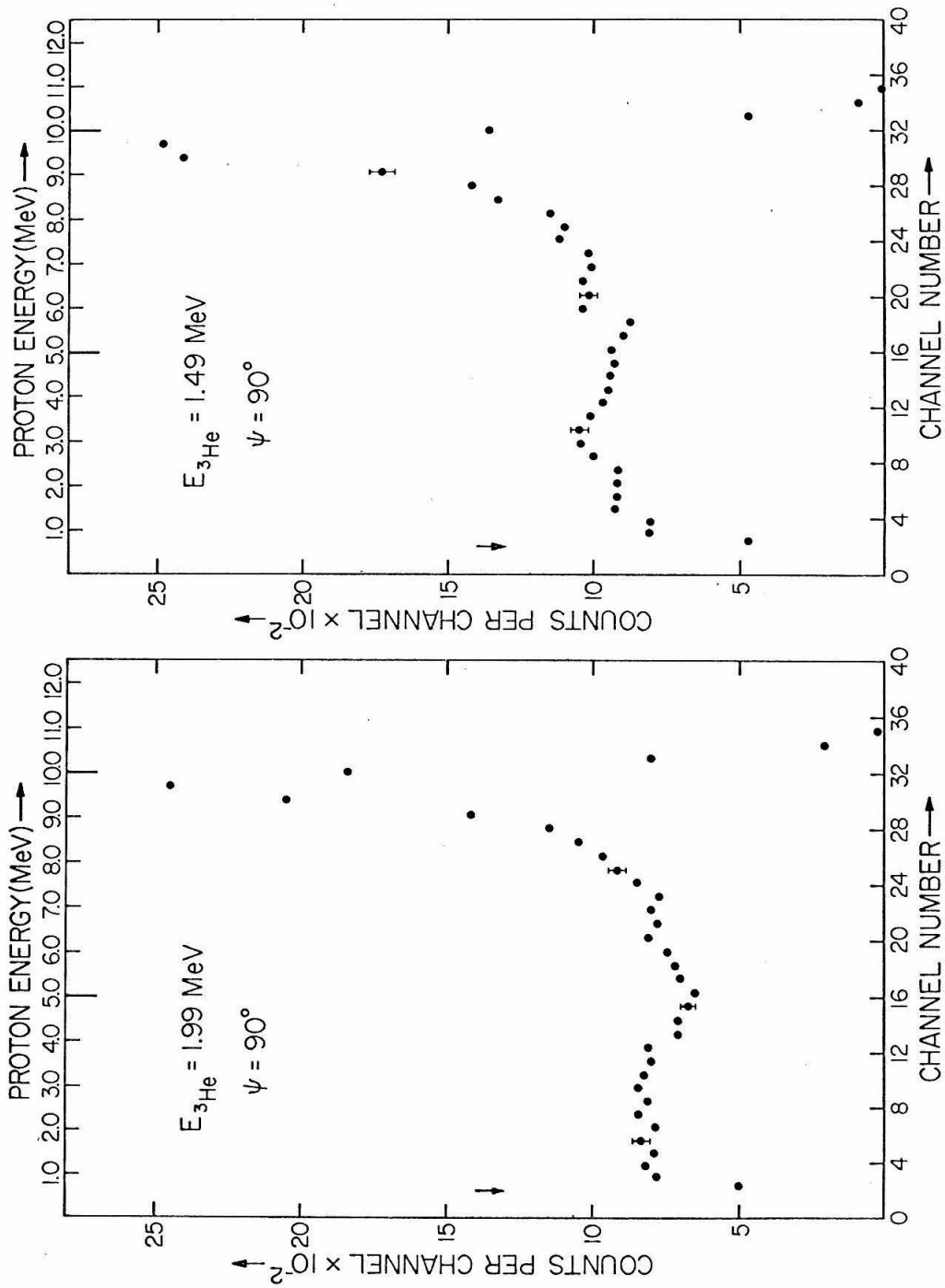
PROTON ENERGY(MeV)
1.0 2.0 3.0 4.0 5.0 6.0 7.0 8.0 9.0 10.0 11.0 12.0
$E_{^3He}$ = 1.49 MeV
ψ = 90°
COUNTS PER CHANNEL × 10^{-2}
25 20 15 10 5
CHANNEL NUMBER
0 4 8 12 16 20 24 28 32 36 40
PROTON ENERGY(MeV)
1.0 2.0 3.0 4.0 5.0 6.0 7.0 8.0 9.0 10.0 11.0 12.0
$E_{^3He}$ = 1.99 MeV
ψ = 90°
COUNTS PER CHANNEL × 10^{-2}
25 20 15 10 5
CHANNEL NUMBER
0 4 8 12 16 20 24 28 32 36 40

FIGURE 11

Proton Spectrum at 1.0 MeV, 90^{o}

(For details see page 101.)

FIGURE 11

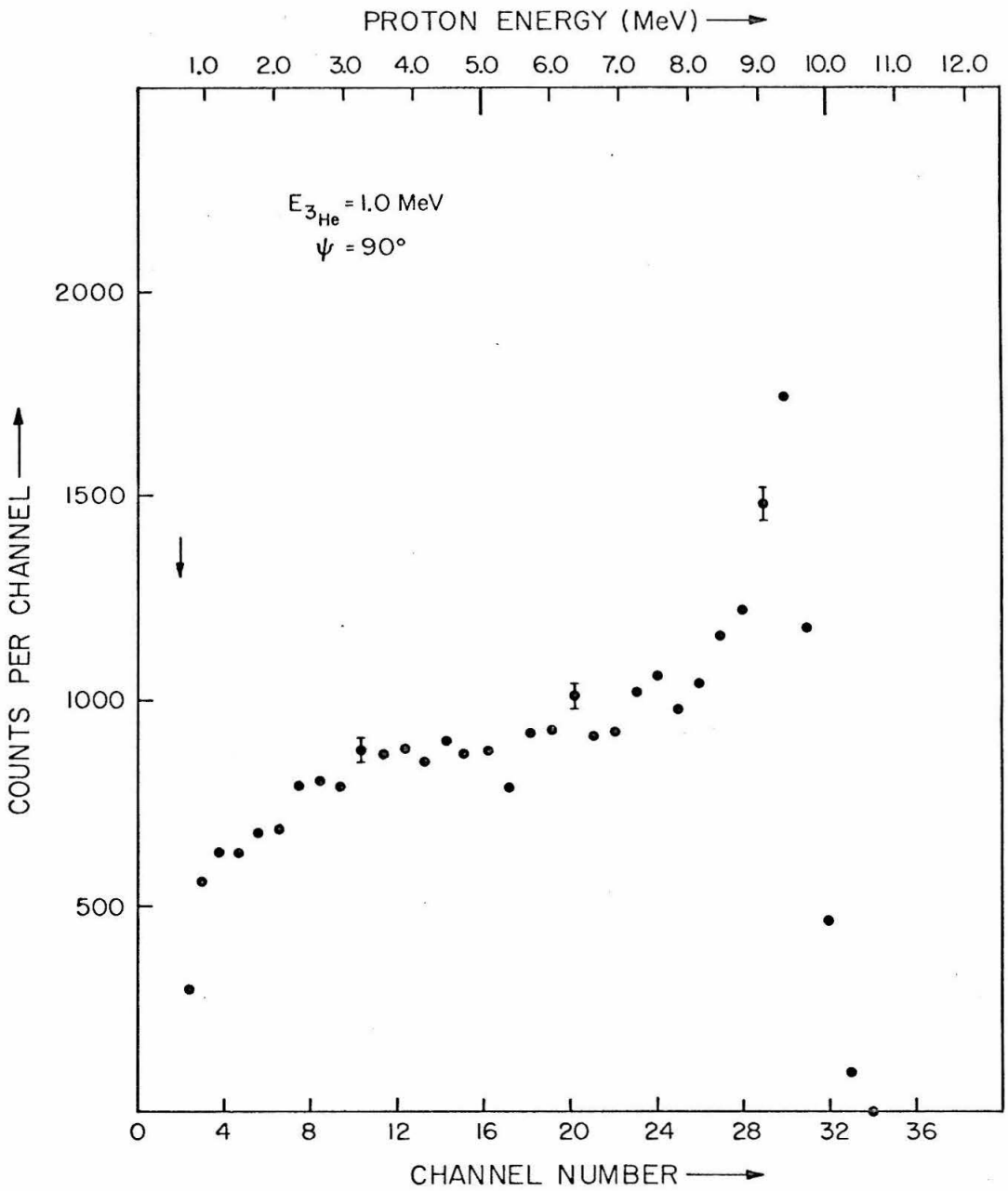
PROTON ENERGY (MeV) ⟶
1.0
2.0
3.0
4.0
5.0
6.0
7.0
8.0
9.0
10.0
11.0
12.0
$E_{^3He}$ = 1.0 MeV
ψ = 90°
COUNTS PER CHANNEL ⟶
2000
1500
1000
500
0
4
8
12
16
20
24
28
32
36
CHANNEL NUMBER ⟶

FIGURE 12

Proton Spectra at 0.79 and 0.59 MeV, 90^{o}

(For details see page 101.)

FIGURE 12

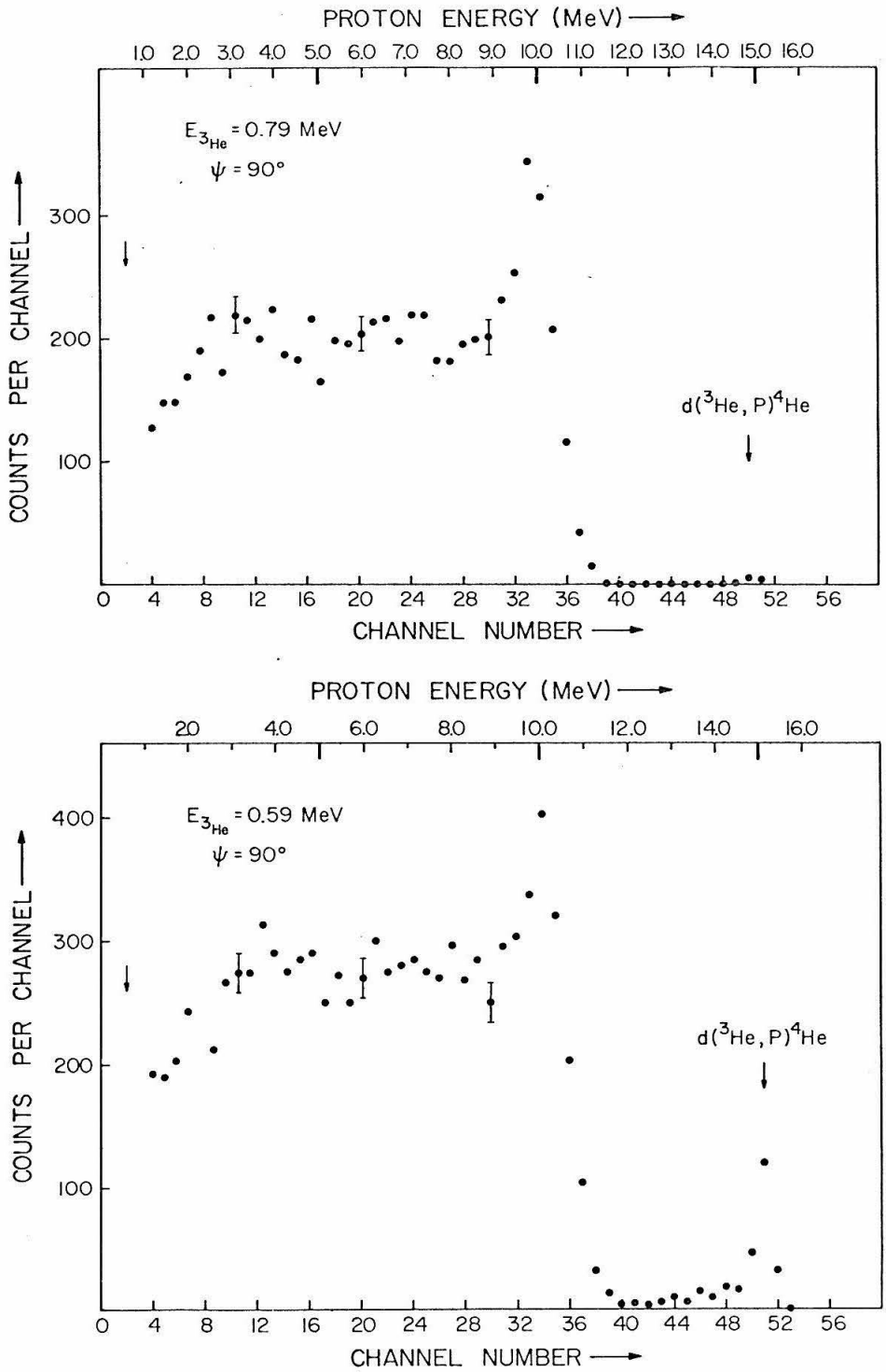
PROTON ENERGY (MeV)
1.0 2.0 3.0 4.0 5.0 6.0 7.0 8.0 9.0 10.0 11.0 12.0 13.0 14.0 15.0 16.0
$E_{^3He}$ = 0.79 MeV
ψ = 90°
d(^{3}He, P)^{4}He
COUNTS PER CHANNEL
100
200
300
0 4 8 12 16 20 24 28 32 36 40 44 48 52 56
CHANNEL NUMBER
PROTON ENERGY (MeV)
2.0 4.0 6.0 8.0 10.0 12.0 14.0 16.0
$E_{^3He}$ = 0.59 MeV
ψ = 90°
d(^{3}He, P)^{4}He
COUNTS PER CHANNEL
100
200
300
400
0 4 8 12 16 20 24 28 32 36 40 44 48 52 56
CHANNEL NUMBER

FIGURE 13

Proton Spectra at 0.49 and 0.30 MeV, 90^{o}

(For details see page 101.)

FIGURE 13

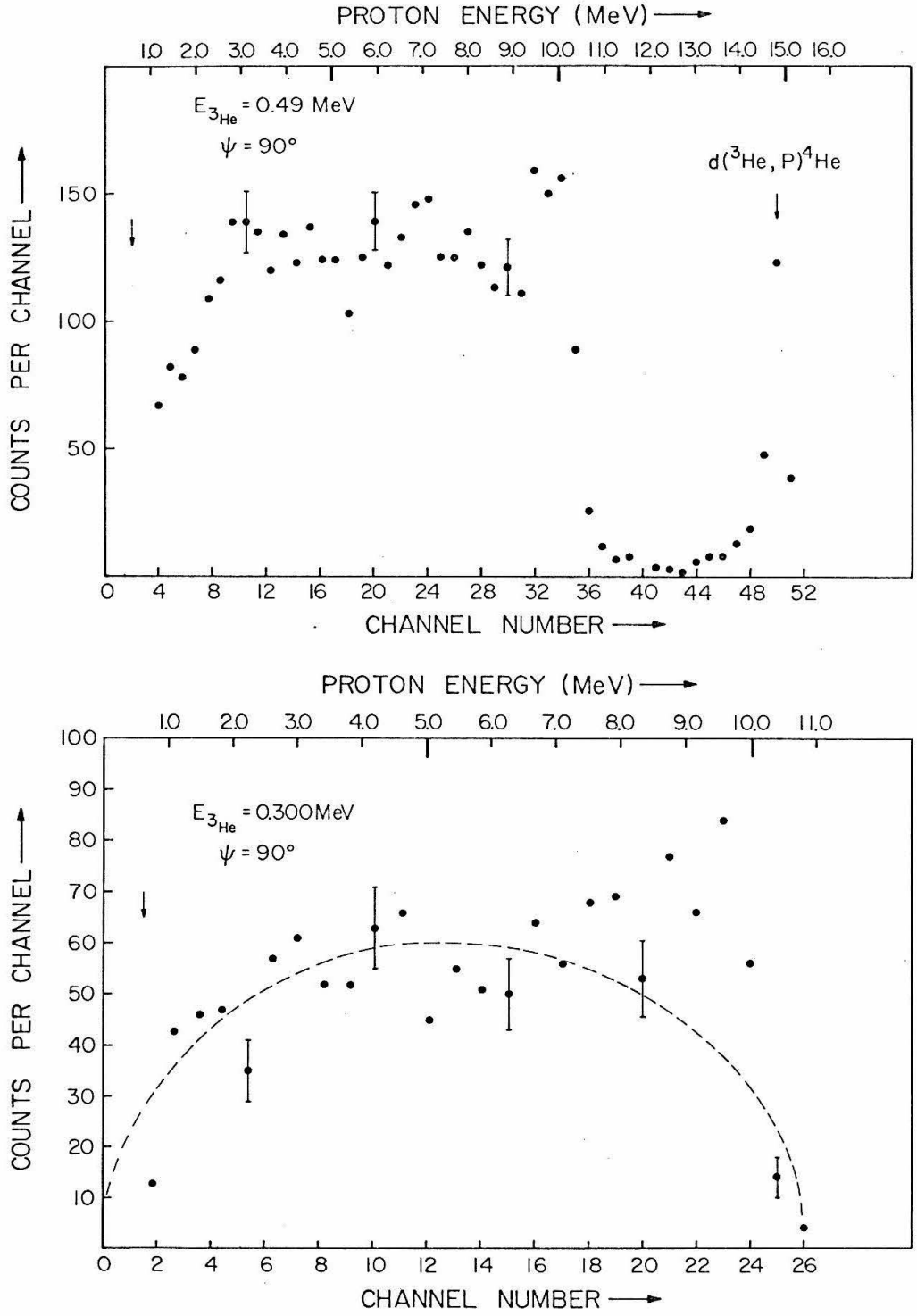
PROTON ENERGY (MeV)
1.0 2.0 3.0 4.0 5.0 6.0 7.0 8.0 9.0 10.0 11.0 12.0 13.0 14.0 15.0 16.0
$E_{^3He}$ = 0.49 MeV
ψ = 90°
d(^{3}He, P)^{4}He
COUNTS PER CHANNEL
150
100
50
0 4 8 12 16 20 24 28 32 36 40 44 48 52
CHANNEL NUMBER
PROTON ENERGY (MeV)
1.0 2.0 3.0 4.0 5.0 6.0 7.0 8.0 9.0 10.0 11.0
$E_{^3He}$ = 0.300MeV
ψ = 90°
COUNTS PER CHANNEL
100 90 80 70 60 50 40 30 20 10
0 2 4 6 8 10 12 14 16 18 20 22 24 26
CHANNEL NUMBER

FIGURE 14

Proton Spectra at 0.30 MeV, 20^{o} and 140^{o}

(For details see page 101.)

FIGURE 14

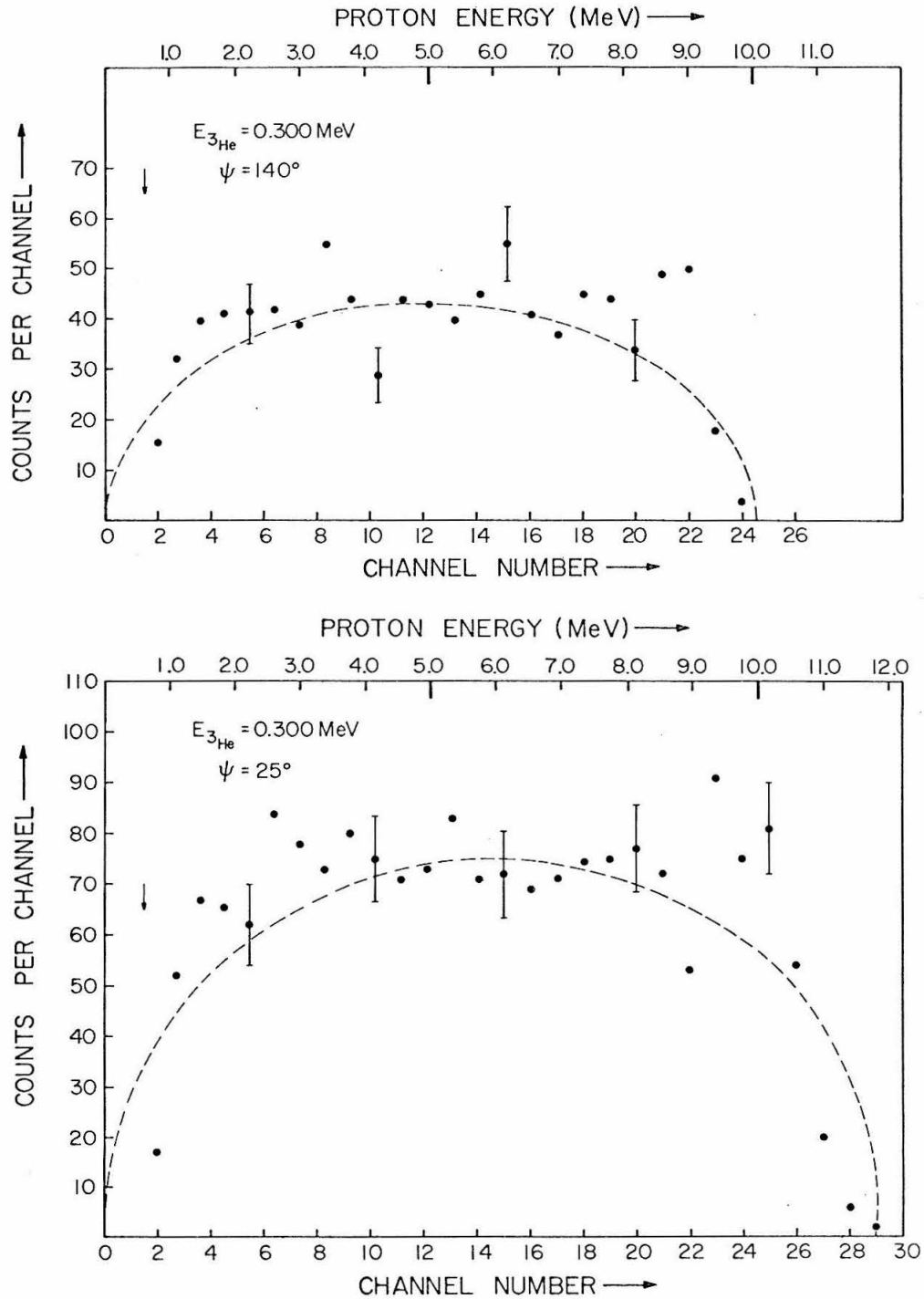
PROTON ENERGY (MeV)
1.0 2.0 3.0 4.0 5.0 6.0 7.0 8.0 9.0 10.0 11.0
$E_{^3He}$ = 0.300 MeV
ψ = 140°
COUNTS PER CHANNEL
CHANNEL NUMBER
PROTON ENERGY (MeV)
1.0 2.0 3.0 4.0 5.0 6.0 7.0 8.0 9.0 10.0 11.0 12.0
$E_{^3He}$ = 0.300 MeV
ψ = 25°
COUNTS PER CHANNEL
CHANNEL NUMBER

FIGURE 15

Proton Spectrum at 0.19 MeV, 90^{o}

(For details see page 101.)

FIGURE 15

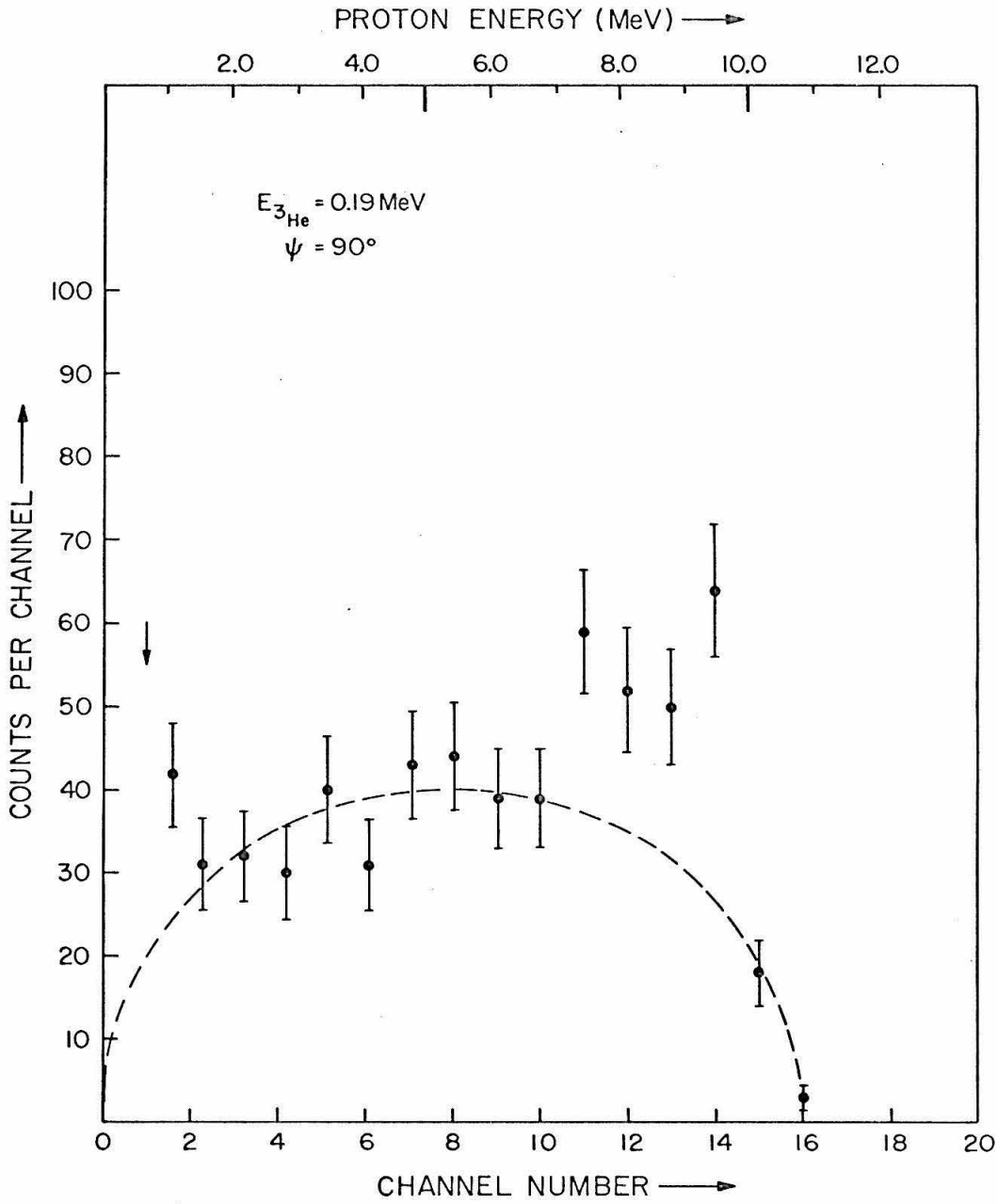
PROTON ENERGY (MeV)
2.0
4.0
6.0
8.0
10.0
12.0
$E_{^3He}$ = 0.19 MeV
ψ = 90°
COUNTS PER CHANNEL
100
90
80
70
60
50
40
30
20
10
0
2
4
6
8
10
12
14
16
18
20
CHANNEL NUMBER

FIGURE 16

Proton Angular Distributions at 2.0 and 1.5 MeV

These figures show proton angular distributions at $E_{^3He}$ = 2.0 and 1.5 MeV, normalized to unity at 90^{o}. The solid curve is the angular distribution calculated by assuming a statistical distribution and isotropic angular distribution in the center-of-mass system. For additional details see pages 29-31.

FIGURE 16

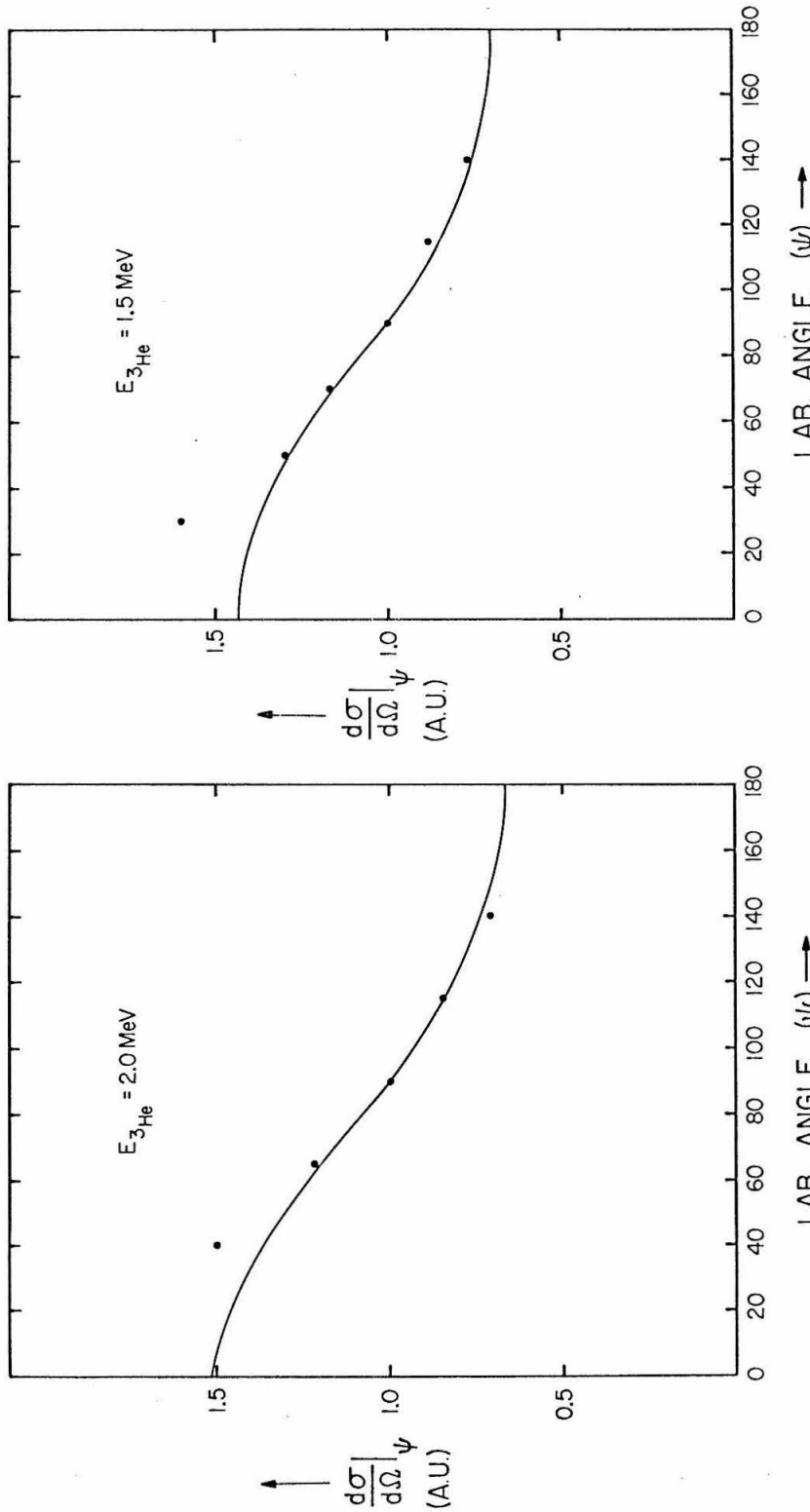
$E_{^3He}$ = 1.5 MeV
$E_{^3He}$ = 2.0 MeV
$\frac{d\sigma}{d\Omega}\Big|_\psi$ (A.U.)
LAB. ANGLE (ψ) ⟶
0
20
40
60
80
100
120
140
160
180
0.5
1.0
1.5

FIGURE 17

Proton Angular Distribution at 1.0 MeV

This figure shows total proton angular distribution at a bombarding energy of 1.0 MeV. The solid curve has the same meaning as in Figure 16. For further details see pages 23-24.

FIGURE 17

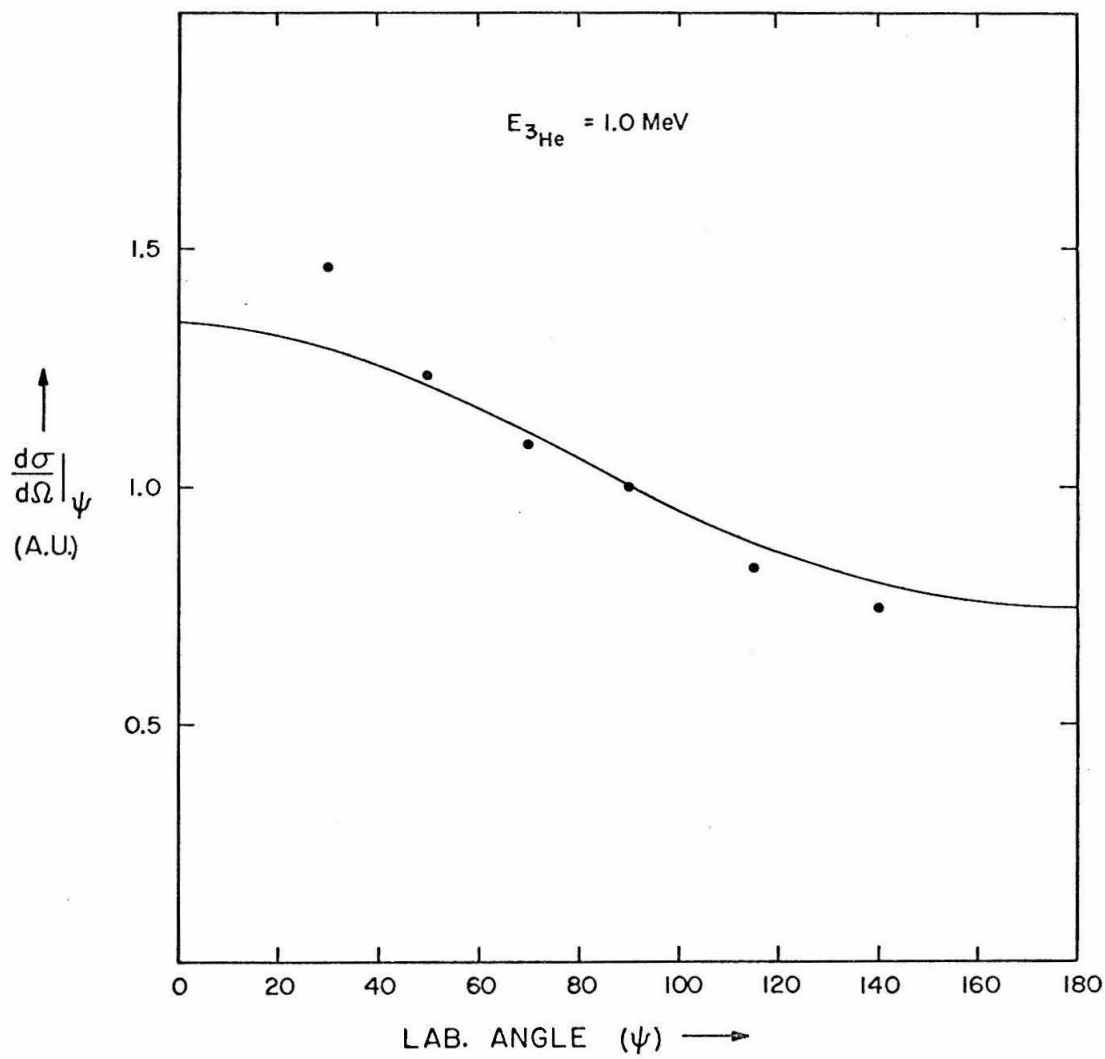
$E_{^3He}$ = 1.0 MeV
1.5
1.0
0.5
$\frac{d\sigma}{d\Omega}\Big|_\psi$
(A.U.)
0
20
40
60
80
100
120
140
160
180
LAB. ANGLE (ψ) ⟶

FIGURE 18

Proton Angular Distributions at 0.743 and 0.300 MeV

The figures show total proton angular distributions at $E_{^3He}$ = 0.743 and 0.300 MeV. A set of two error bars is indicated at a couple of points. The larger error bar indicates the absolute error in the differential cross section determination, while the smaller error bar (Heavier line) indicates the relative error between two points. The solid line has the same meaning as in Figure 16. For further details see pages 23-24.

FIGURE 18

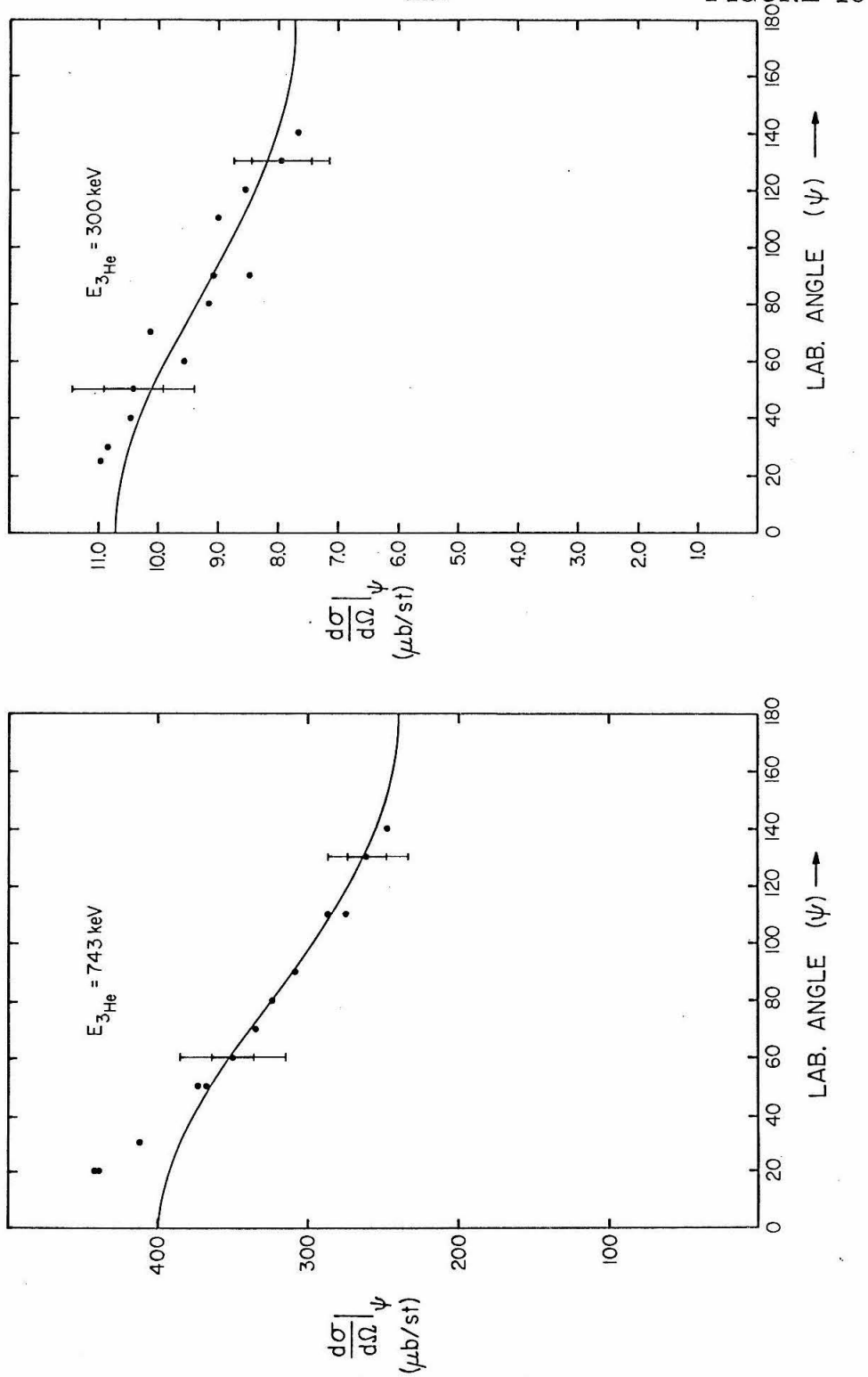
$E_{^3He}$ = 743 keV
$E_{^3He}$ = 300 keV
$\frac{d\sigma}{d\Omega}\Big|_\psi$ (μb/st)
LAB. ANGLE (ψ) ⟶
0
20
40
60
80
100
120
140
160
180
100
200
300
400
1.0
2.0
3.0
4.0
5.0
6.0
7.0
8.0
9.0
10.0
11.0

FIGURE 19

Alpha Spectra at 1.495 and 0.955 MeV, 30^{o}

The figures show the alpha particle spectra at 1.495 and 0.955 MeV and 30^{o} to the incident beam. The arrow indicates the lower limit of the alpha particle energies observed by the counter telescope. Typical counting statistics are shown for a few points. See page 24.

FIGURE 19

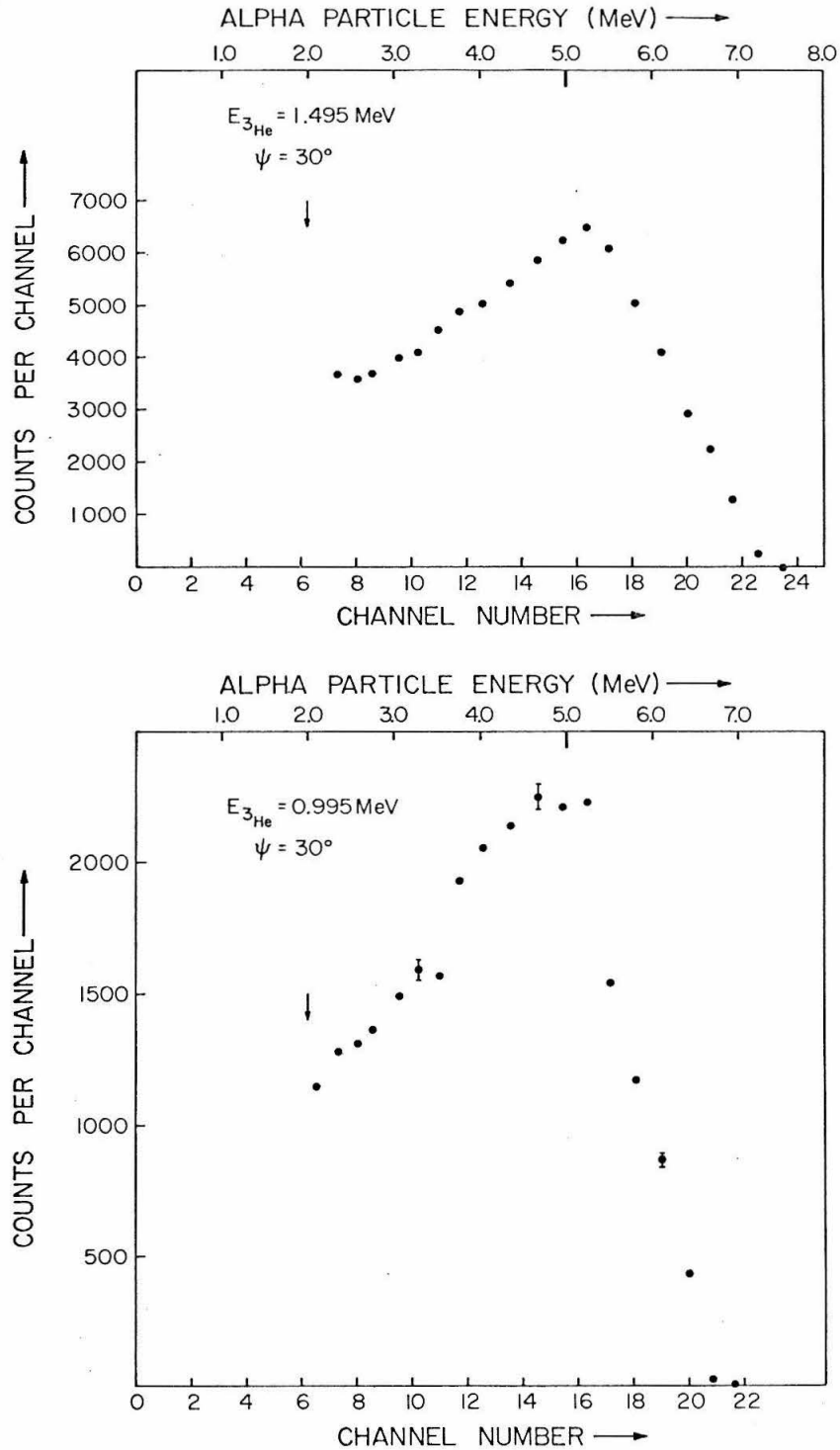
ALPHA PARTICLE ENERGY (MeV) ⟶
1.0 2.0 3.0 4.0 5.0 6.0 7.0 8.0
$E_{^3He}$ = 1.495 MeV
ψ = 30°
COUNTS PER CHANNEL ⟶
7000
6000
5000
4000
3000
2000
1000
0 2 4 6 8 10 12 14 16 18 20 22 24
CHANNEL NUMBER ⟶
ALPHA PARTICLE ENERGY (MeV) ⟶
1.0 2.0 3.0 4.0 5.0 6.0 7.0
$E_{^3He}$ = 0.995 MeV
ψ = 30°
COUNTS PER CHANNEL ⟶
2000
1500
1000
500
0 2 4 6 8 10 12 14 16 18 20 22
CHANNEL NUMBER ⟶

FIGURE 20

Alpha Spectrum at 0.743 MeV and 20^{o}

This figure shows an alpha spectrum at 0.743 MeV and 20^{o} in the laboratory. Details are as in Figure 19 (page 120).

FIGURE 20

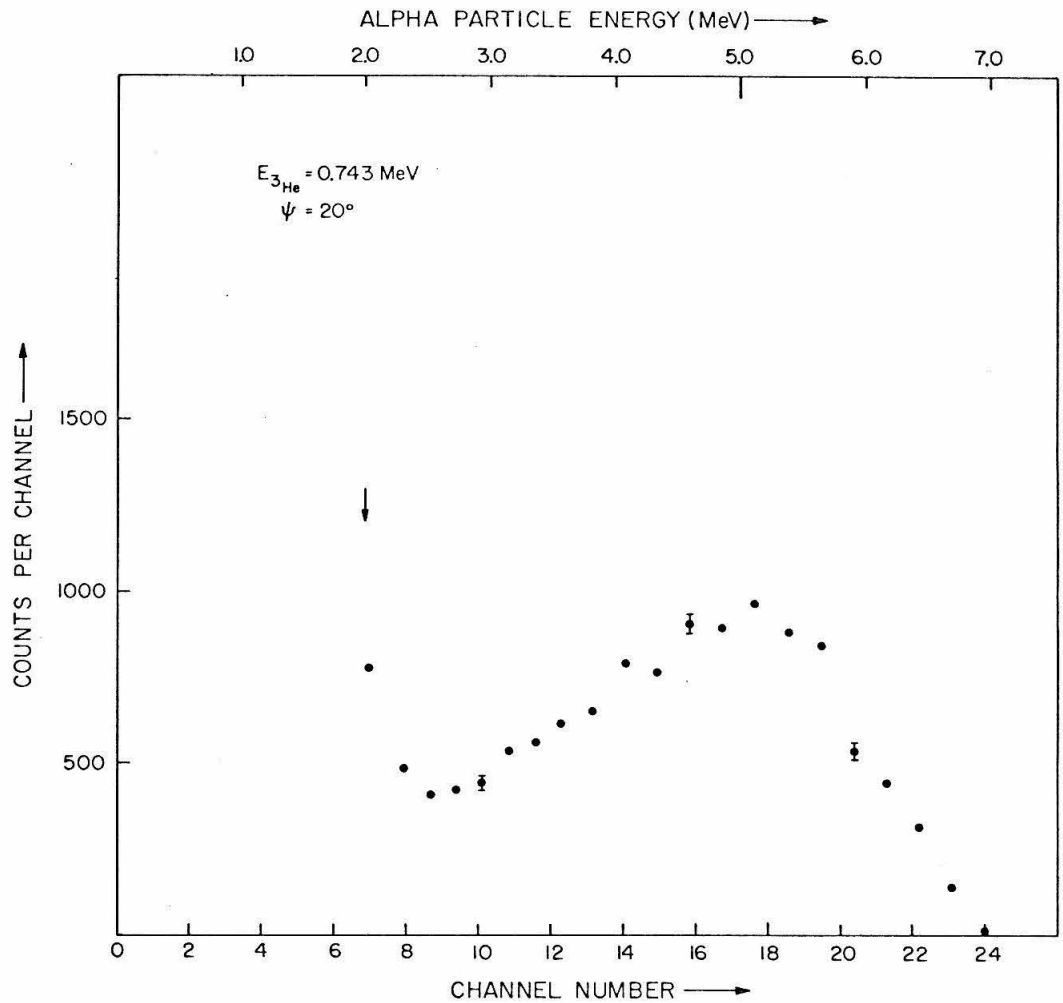
ALPHA PARTICLE ENERGY (MeV)
1.0
2.0
3.0
4.0
5.0
6.0
7.0
$E_{^3He}$ = 0.743 MeV
ψ = 20°
COUNTS PER CHANNEL
1500
1000
500
0
2
4
6
8
10
12
14
16
18
20
22
24
CHANNEL NUMBER

FIGURE 21

$^{3}He(^{3}He, 2p)^{4}He$ Total Cross Sections

The total cross sections for the reaction $^{3}He(^{3}He, 2p)^{4}He$ reaction are given as a function of the center-of-mass energy. Typical absolute errors (Systematic and Statistical) associated with individual measurements are +13% and -9%. The solid line is a smooth curve through the data points. For details see pages 29-30.

FIGURE 21

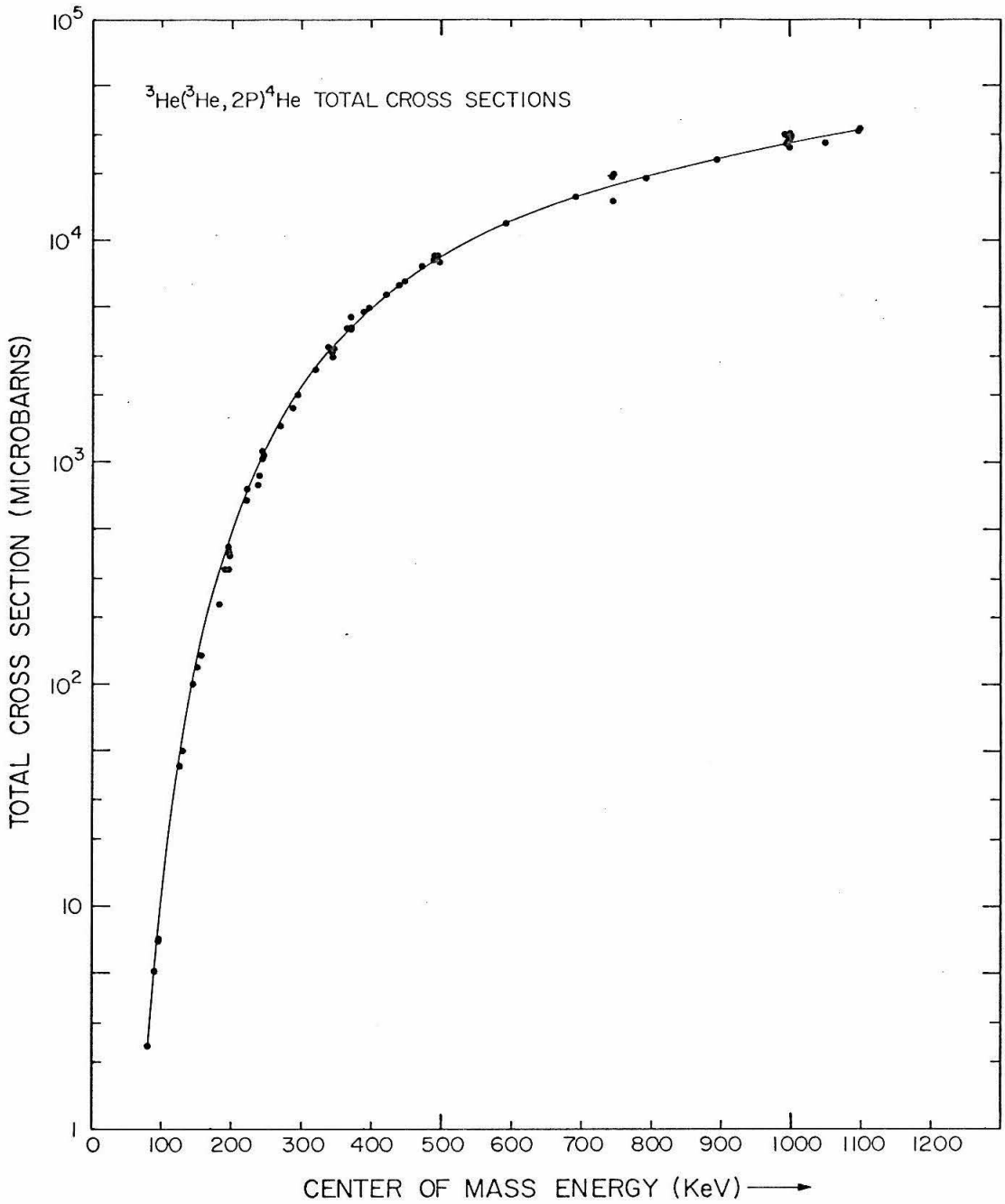
$^3He(^3He, 2P)^4He$ TOTAL CROSS SECTIONS
TOTAL CROSS SECTION (MICROBARNS)
10^5
10^4
10^3
10^2
10
1
0
100
200
300
400
500
600
700
800
900
1000
1100
1200
CENTER OF MASS ENERGY (KeV) ⟶

FIGURE 22

$^{3}He(d, p)^{4}He$ Differential Cross Sections at 90^{o}

The $^{3}He(d, p)^{4}He$ differential cross sections at 90^{o} in the laboratory are plotted as a function of the deuteron energy. Typical absolute (Statistical and Systematic) errors in the differential cross section are estimated to be +10%, -7%. The solid line is a smooth curve through the data points. The triangular data symbols are from the measurements of Yarnell et al. (1953). For additional details see page 32.

FIGURE 22

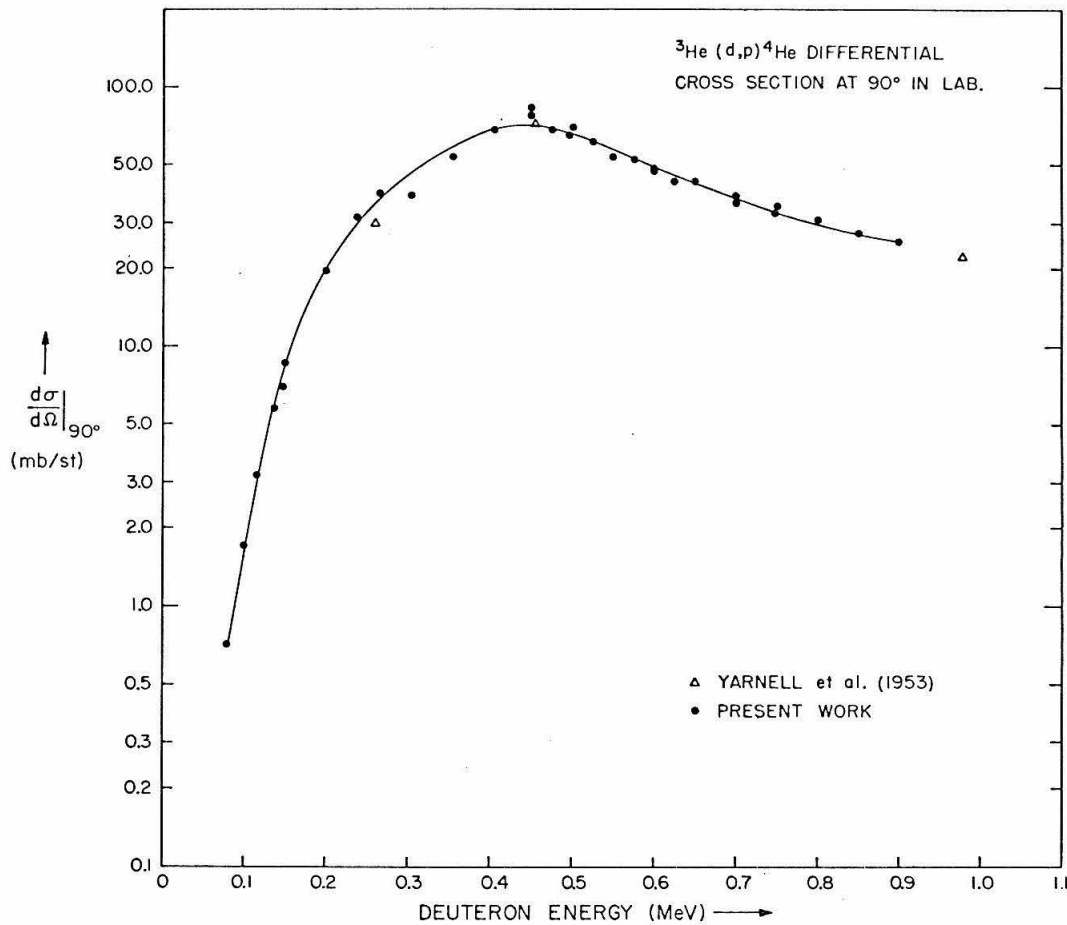
^{3}He (d,p)^{4}He DIFFERENTIAL
CROSS SECTION AT 90° IN LAB.
100.0
50.0
30.0
20.0
10.0
5.0
3.0
2.0
1.0
0.5
0.3
0.2
0.1
$\frac{d\sigma}{d\Omega}\Big|_{90°}$
(mb/st)
0
0.1
0.2
0.3
0.4
0.5
0.6
0.7
0.8
0.9
1.0
1.1
DEUTERON ENERGY (MeV) ⟶
△ YARNELL et al. (1953)
• PRESENT WORK

FIGURE 23

$^{3}He(^{3}He, 2p)^{4}He$ Cross Section Factors

The $^{3}He(^{3}He, 2p)^{4}He$ cross section factors $[S(E) = \sigma(E) \cdot E \cdot \exp(2\pi\eta)]$ are plotted as a function of the energy in the center-of-mass system. Total errors (Statistical and Systematic) are indicated for a few representative points. Also shown are the cross section factors calculated from the total cross section measurements for this reaction by Good et al. (1953), Neng-Ming et al. (1966) and by Bacher and Tombrello (1967). A representative error bar is shown for the data of Bacher and Tombrello at $E_{cm} \sim 700$ keV. For a detailed discussion of these, see pages 30-31.

FIGURE 23

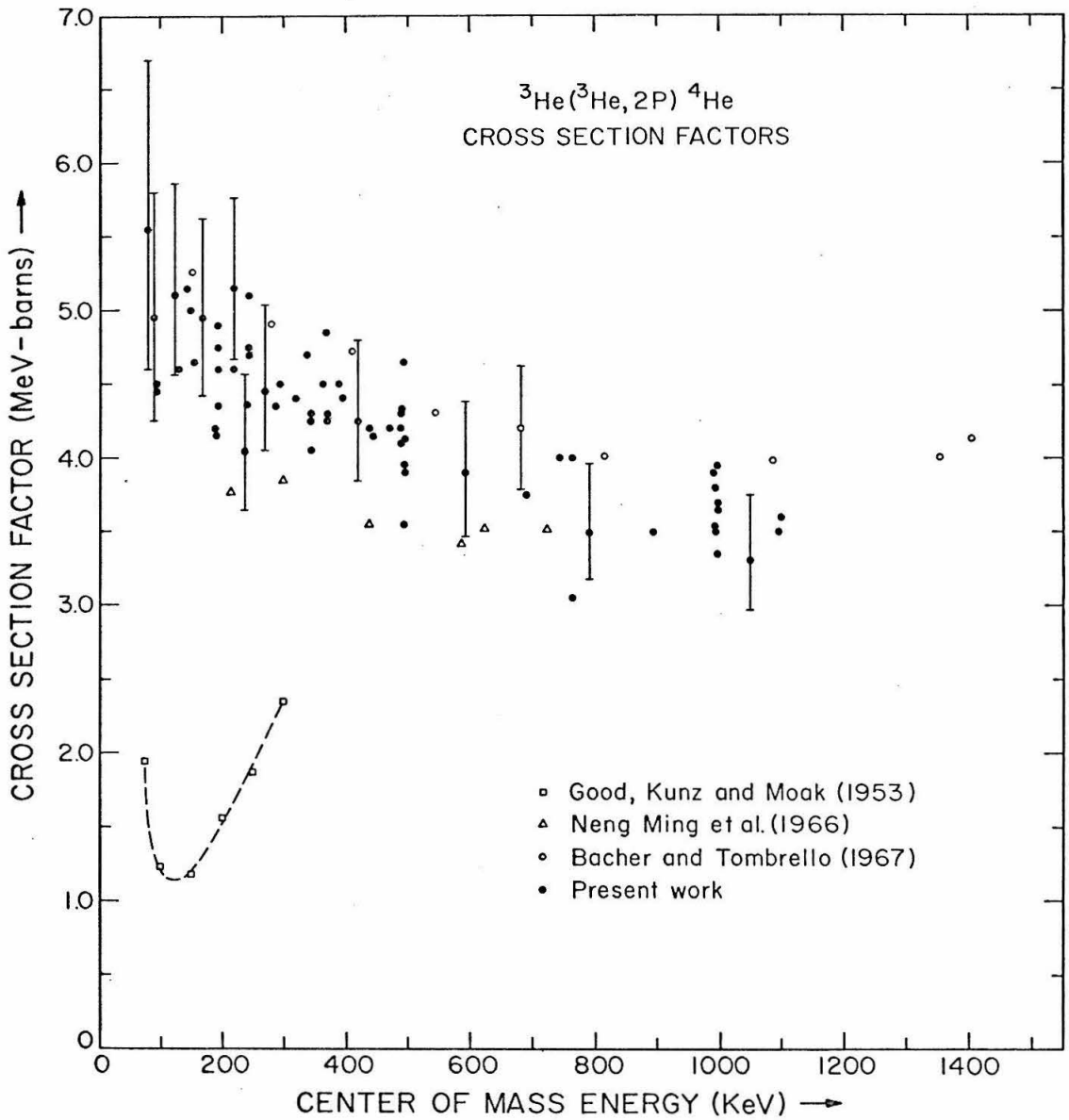
$^3He(^3He, 2P)\ ^4He$
CROSS SECTION FACTORS
CROSS SECTION FACTOR (MeV-barns) →
CENTER OF MASS ENERGY (KeV) →
0
1.0
2.0
3.0
4.0
5.0
6.0
7.0
0
200
400
600
800
1000
1200
1400
Good, Kunz and Moak (1953)
Neng Ming et al. (1966)
Bacher and Tombrello (1967)
Present work

FIGURE 24

$\Sigma(E)$ for $^3He + {}^3He \rightarrow {}^4He + 2p$

$\Sigma(E)$, closely related to the cross section factor $S(E)$ is given by

$$\Sigma(E) = \sigma(E)/E \left[\frac{1}{F_0^2(kR_0) + G_0^2(kR_0)} + \frac{9}{F_1^2(kR_1) + G_1^2(kR_1)} \right]$$

for the $^3He + {}^3He$ reaction. The figure shows a plot of $\Sigma(E)$ as a function of the energy in the center-of-mass system for the radius parameters $R_0 = 3.7$ fermies and $R_1 = 3.0$ fermies. The triangular data symbol at about 1.4 MeV is from the measurements of Bacher (1967). The dashed line indicates the average value of $\Sigma(E)$. For further details see pages 42-44.

FIGURE 24

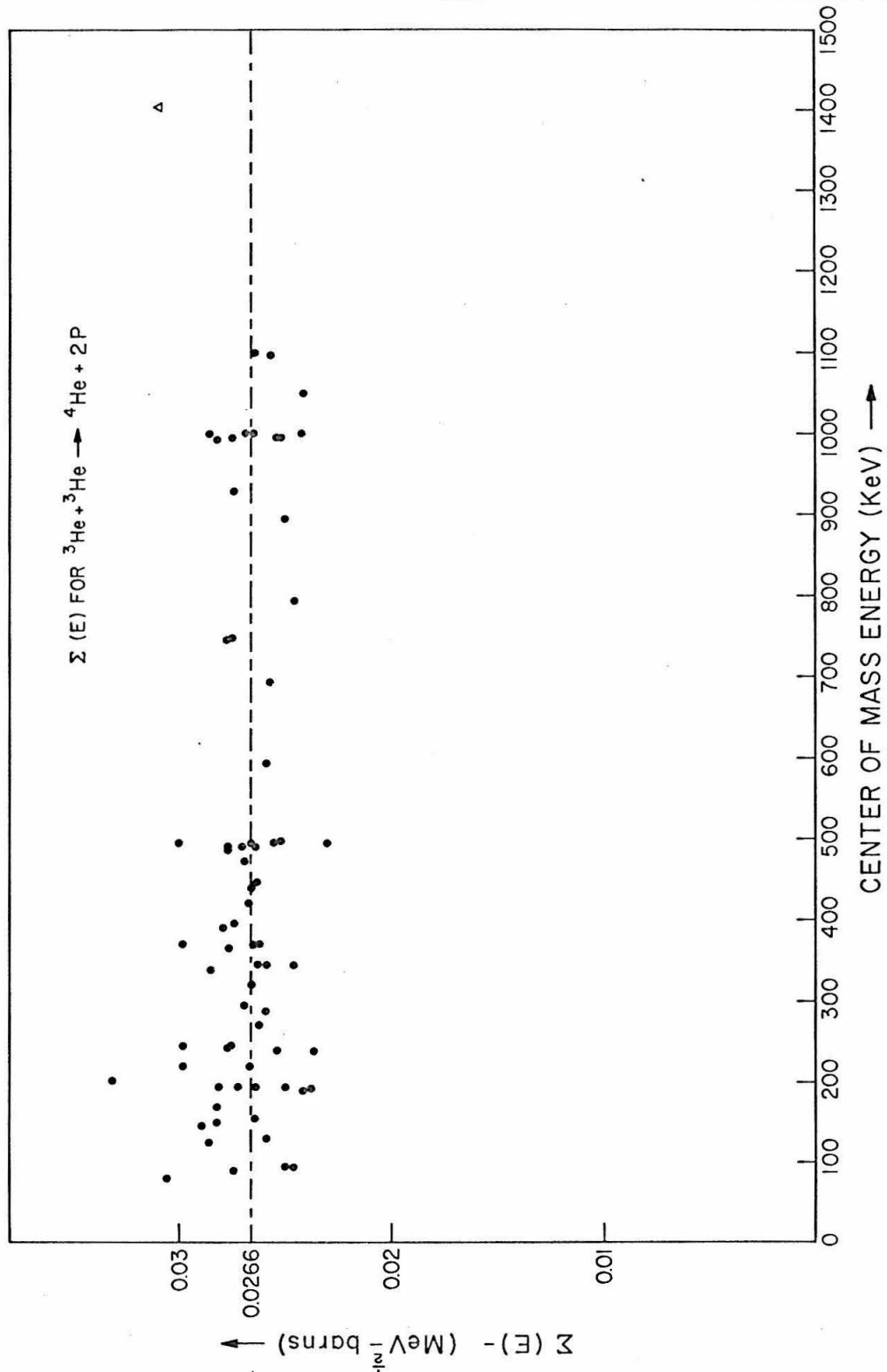
Σ (E) FOR $^3He + ^3He \rightarrow ^4He + 2P$
Σ (E) - (MeV^{-1} barns)
0.03
0.0266
0.02
0.01
0
100
200
300
400
500
600
700
800
900
1000
1100
1200
1300
1400
1500
CENTER OF MASS ENERGY (KeV)

FIGURE 25

$\Sigma(E)$ for (3 + 3) Reactions

This figure shows a plot of $\Sigma(E)$ vs. E, the center-of-mass energy for reactions between A = 3 nuclei. For the $^3He(^3He, 2p)^4He$ and the $T(T, 2n)^4He$ reactions $\Sigma(E)$ is given by:

$$\Sigma(E) = \sigma(E)\sqrt{E}\left[\frac{1}{F_0^2(kR_0)+G_0^2(kR_0)} + \frac{9}{F_1^2(kR_1)+G_1^2(kR_1)}\right].$$

For the reaction between ^3He and T, the total cross section and the partial cross section for $^3He(T, np)^4He$ are separately fitted and the $\Sigma(E)$ for these two processes is given by:

$$\Sigma(E) = \sigma(E)\sqrt{E}\left[\frac{2}{F_0^2(kR_0)+G_0^2(kR_0)} + \frac{6}{F_1^2(kR_1)+G_1^2(kR_1)}\right].$$

All the fits use the same values for R_0(= 3.7 fm) and R_1 (= 3.0 fm). For the $^3He(^3He, 2p)^4He$ reaction the average value of $\Sigma(E)$ is indicated. For further details see pages 42-45.

FIGURE 25

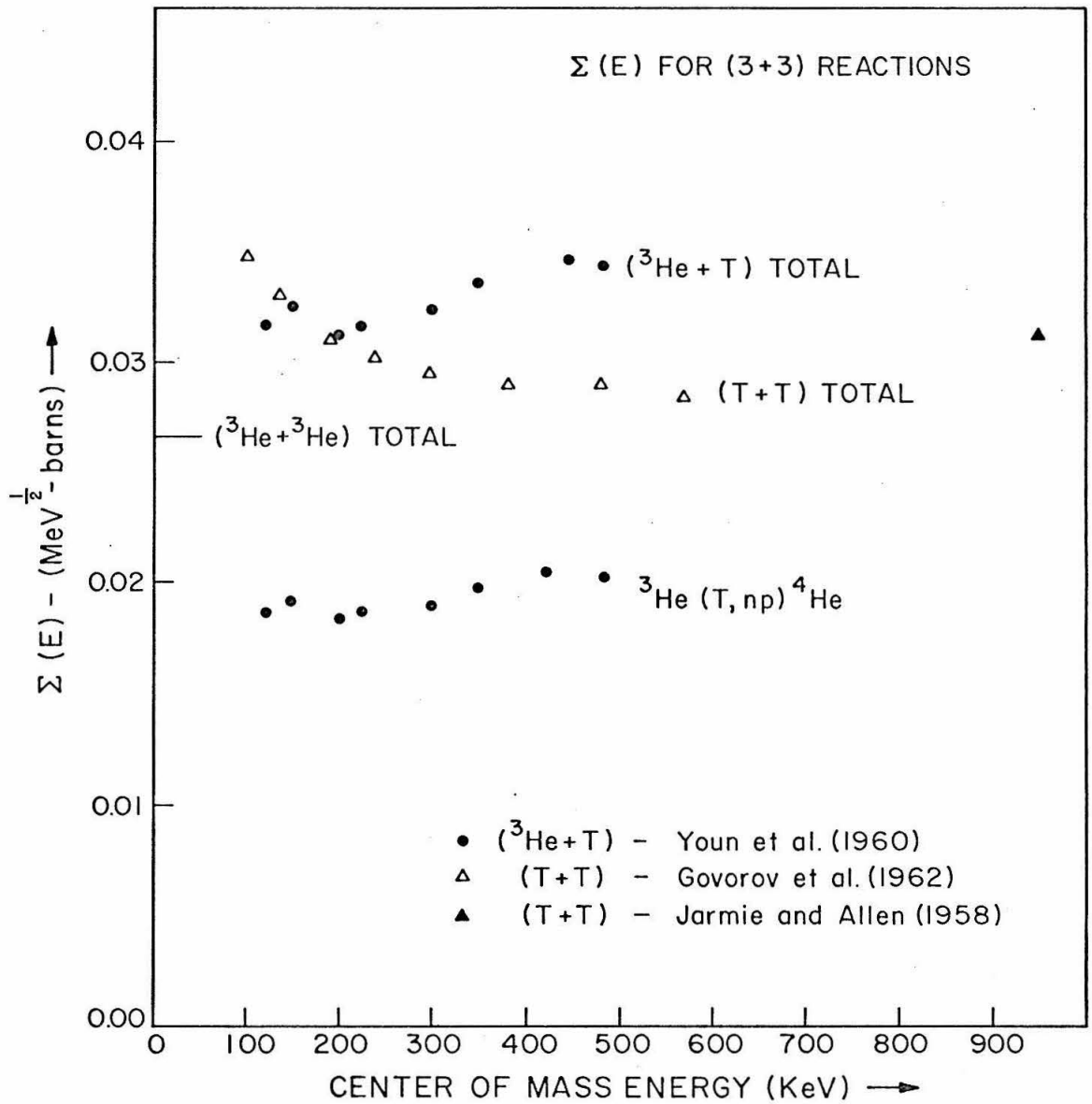
Σ (E) FOR (3+3) REACTIONS
0.04
0.03
0.02
0.01
0.00
Σ (E) - (MeV$^{-\frac{1}{2}}$ - barns)
(^{3}He + T) TOTAL
(T+T) TOTAL
(^{3}He+^{3}He) TOTAL
^{3}He (T, np) ^{4}He
(^{3}He+T) - Youn et al. (1960)
(T+T) - Govorov et al. (1962)
(T+T) - Jarmie and Allen (1958)
0
100
200
300
400
500
600
700
800
900
CENTER OF MASS ENERGY (KeV)